Biophysical dissection of SOX18/NR2F2 transcriptional antagonism reveals mechanisms of venous differentiation and drug action in vascular malformation

Matthew S. Graus[1,2]*, Sawan Kumar Jha[3]*, Jieqiong Lou[4], Annegret Holm[5], Yew Yan Wong[1,2], Tara Davidson[1,2], Paul Coleman[1], Ella Sugo[6], Winnie Luu[1], Tara Karnezis[7], Jennifer Gamble[1], Geoff McCaughan[2], Scott Nightingale[6], Joyce Bischoff[5], Kazuaki Maruyama[8], Elizabeth Hinde[4], Kristy Red-Horse[3,9,10,11]†*and Mathias Francois[1,2]†*

[1] The University of Sydney, School of Medical Sciences, Sydney, New South Wales, 2006, Australia.

[2] The Centenary Institute, The Genome Imaging Centre, Royal Prince Alfred Hospital, Sydney, New South Wales, 2006, Australia.

[3] Stanford University, Department of Biology, Clark Center, 318 Campus Drive, Stanford, E350, CA 94305, USA.

[4] The University of Melbourne, School of Physics, Melbourne, Victoria, 3010, Australia.

[5] Vascular Biology Program, Department of Surgery, Boston Children's Hospital, Harvard Medical School, Boston, MA, United States

[6] Hunter New England Health, John Hunter Hospital, Lookout Road, New Lambton Heights, NSW 2305, Australia.

[7] Gertrude Biomedical Pty Ltd., Bio21, Melbourne, Victoria, Australia.

[8] Department of Pathology and Matrix Biology, Graduate School of Medicine, Mie University
2-174 Edobashi, Tsu, Mie 514-8507, Japan.

[9] Stanford Cardiovascular Institute, Stanford, CA 94305, USA.

[10] Institute for Stem Cell Biology & Regenerative Medicine, Stanford University, Stanford, CA 94305, USA.

[11] Howard Hughes Medical Institute, USA.

*Authors have contributed equally to this work

†Correspondence should be address to

Kristy Red-Horse (Tel: +81-92-642-6882)

kredhors@stanford.edu

Mathias Francois (Tel: +61 28627 9497)

mathias.francois@sydney.edu.au

One-sentence summary: Antagonistic interplay between SOX18 and NR2F2 allows therapeutic rescue of a rare NR2F2 mutation syndrome using a SOX18 inhibitor.

Keywords: transcription drug, SOX18, NR2F2, transcription factor, transcription factor antagonism, live imaging, single molecule, stem cell, repurposing, vascular anomalies, endothelial cell

Abstract

Translating genomic discoveries into therapies for rare genetic disorders remains a significant challenge, particularly for variants of unknown significance (VUS) where molecular mechanisms are unclear. This is particularly relevant in vascular malformations, where venous differentiation remains poorly understood, and the role of transcription factors in specifying venous identity is only beginning to be elucidated.

Here, we combine live-cell single-molecule imaging with genomics-based approaches to uncover a biophysical mechanism of transcription factor antagonism that underpins venous identity. We show that SOX18 and NR2F2 antagonistically co-regulate venous differentiation through dynamic feedback between their nuclear populations. This interaction is disrupted in vascular malformation syndrome caused by a *de novo* heterozygous *NR2F2* mutation, presenting with aberrant vascular integrity and bleeding. Treatment with an FDA-approved drug—known to inhibit SOX18—led to marked clinical improvement in the proband.

To dissect the molecular mechanism underlying this mutation and the drug response, we used human embryonic stem cells (hESCs) engineered to carry the proband's NR2F2 variant. These cells exhibited impaired hESC to venous differentiation with no effect on artery EC differentiation. *In silico* modelling and live-cell molecular imaging revealed that the NR2F2 variant is hyper-mobile, fails to form homodimers, and cannot recruit SOX18, thereby disrupting a critical transcriptional antagonism that underpins venous endothelial identity. We demonstrate that targeted pharmacological inhibition of SOX18 restores this regulatory balance in hESC-derived venous endothelial cells, rescuing both gene expression and NR2F2 binding dynamics at the single-molecule level. Together, this study uncovers a biophysical mechanism of transcription factor antagonism that governs venous differentiation and offers a framework for developing targeted therapies for rare vascular malformations.

Introduction

Venous differentiation during development is a complex process governed by a network of transcription factors (TFs) that orchestrate the specification and maturation of venous endothelial cells. Despite significant advances in our understanding of arterial and venous identity, knowledge gaps persist regarding the precise regulatory mechanisms and interactions among TFs involved in venous lineage commitment. Notably, the interplay between SOX18 and NR2F2 TFs has emerged as a critical area of study, as these factors appear to play complementary roles in defining venous and lymphatic endothelium identity. Understanding this interplay may provide insights into the molecular underpinnings of vascular development and potential therapeutic targets for vascular-related diseases.

The nuclear receptor subfamily 2 group F member 2 (COUPTFII/NR2F2) is a TF required for vein development in embryonic mice, zebrafish and xenopus[1–5]. Genetic disruption approaches have demonstrated that homozygous loss of NR2F2 is embryonically lethal, and heterozygous loss is attributed to vascular anomalies[6,7]. It can also block the natural vein to artery transition required for coronary artery formation[8]. Although little is known about its function in human vein development, NR2F2 may be essential for life since it has a probability of being loss-of-function intolerant (pLI = 0.99, Genome Aggregation Database (gnomAD) v 4.1.0). Due to the inflexibility of NR2F2 variants, many are associated with or are genetic components of several human diseases, including congenital heart disease[9–11] and congenital diaphragmatic hernia[12], among other developmental defects[13].

Evidence shows that NR2F2 supports venous endothelial cell (EC) differentiation though two potential mechanisms: 1. Regulating cell identity genes—promoting venous and inhibiting arterial genes[1,14,15] and 2. enhancing cell cycle genes[8,14,15]. Deletion of one copy in coronary ECs during embryonic development drastically decreases EC numbers and proliferative capabilities[8]. Interactions with protein partners, such as GATA2 or NKX2-3, modulate part of NR2F2 activity[16,17]. In addition, the *Nr2f2* and *Sox18* genetic pathways cooperate in venous progenitor cells[18], to initiate the early steps of lymphatic EC specification[19] through the direct control of *Prox1* gene transactivation.

SOX18 is a member of the SOX (SRY-related HMG-box) family of TFs that is essential for different aspects of EC differentiation. It has been shown to regulate vessel calibre via genetic cross talk with VEGF-D[20] and influences the regulation of EC contact[21,22]. During embryogenesis, SOX18 expression is essential to induce the early steps of lymphatic specification, partly through the induction of *Prox1* transcription[23]. Its expression is subsequently downregulated once the blood and lymphatic vascular networks are established. However, the interplay between NR2F2 and SOX18 TFs to coordinate and modulate their activities in veins and lymphatic ECs remains elusive.

Under pathological conditions in adults, SOX18 is reactivated and plays a role in modulating endothelial progenitor cell differentiation during solid tumour growth[24–26]. Consequently, mutations in SOX18 have been identified for their involvement in rare human vascular disorders, including hypotrichosis-lymphedema-telangiectasia-renal syndrome (HLTRS) [27,28] and cancer metastasis[29]. Beyond these conditions, SOX18 has also been shown to play a role in the formation of abnormal vasculature as seen in infantile hemangioma (IH), a vascular neoplasm characterized by rapidly growing, aberrant vessels. Notably, SOX18 is a key regulator of hemangioma stem cells to hemangioma endothelial cell differentiation[30,31]. This mechanism is further supported by the development of a small molecule inhibitor, SM4[18,32] and the evidence that two FDA-approved therapies (propranolol and atenolol) are currently used to treat IH[30,31,33], providing compelling evidence of SOX18's involvement in pathological ECs differentiation and highlighting its potential as a therapeutic target.

Failure of these two TFs to carry out their functions often leads to lethal outcomes, due to defects that impair the cardio-vascular system and endothelial cell differentiation or function[34,35]. Here, we focus on a young proband with new *de novo* mutation in NR2F2 and the functional characterisation of this genetic insult at the molecular and cellular levels. *De novo* genetic variants have been implicated in the development of vascular malformations, with a prevalence of 1.2% to 1.5% in children[36,37]. Each disease needs to be assessed individually to identify genetic vulnerabilities and elucidate the etiological components, thereby determining treatment options. For this reason, developing assays to perform functional validation alongside next-generation sequencing technologies is essential to discovering biology associated with variants of unknown significance (VUS) and, therefore, potentially providing patients with personalized therapeutic options. There is a growing interest in VUS that alter the activity of genome effectors such as TFs, which are key molecular switches essential to proper embryonic development. TFs often operate within combinatorial networks, where opposing activities fine-tune lineage specification and gene expression. A classic example is the mutual antagonism between PU.1 and GATA1 in hematopoiesis[38,39], where each TF represses the other's activity to direct lineage choice. Similarly, the opposing functions of FOXO and MYC regulate the balance between cellular quiescence and proliferation[40], while SOX2 and TCF/LEF factors exert context-dependent control over Wnt-responsive enhancers during early development[41]. These mechanisms exemplify how TFs can co-occupy shared regulatory elements yet drive divergent outcomes.

Here, we uncover an antagonistic co-regulation between SOX18 and NR2F2 essential for venous endothelial identity, by combining next-generation sequencing, *in silico* modelling, and quantitative live-cell molecular imaging. This integrated approach reveals TFs coordinated activity which disruption underlies a rare vascular syndrome. To investigate the functional consequences of a de novo heterozygous NR2F2 variant of unknown significance (VUS) identified in a proband with vascular anomalies, we employed a human embryonic stem cell (hESC) - to vascular endothelial cell (hVEC)

differentiation model[42]. Notably, the proband exhibited clinical improvement following treatment with propranolol—a drug with known off-target inhibitory activity against SOX18—which led us to explore whether pharmacological disruption of SOX18 could compensate for the dysfunction of NR2F2.

Our molecular approach reveals that the VUS results in a loss-of-function NR2F2 protein that impairs venous endothelial differentiation by disrupting its interaction with SOX18, thereby uncoupling the transcriptional antagonism essential for balanced gene regulation that maintains venous identity. This mechanistic insight prompted us to test whether SOX18 inhibition could restore a transcriptional balance and phenotypic rescue. Using hESC-derived hVECs and single-molecule imaging, we demonstrate that pharmacological blockade of SOX18 functionally compensates for the NR2F2 mutation, providing proof of concept for targeted intervention via modulation of transcription factor interplay.

149 **Results**

150 **NR2F2 and SOX18 influence each other's molecular behavior**

151 Despite pervious characterization of the genes regulated by *Sox18* and *Nr2f2* during endothelial cell
152 development[4,43], there is little understanding of how these two TFs biophysically and biochemically
153 operate to instruct gene transcription of the venous or lymphatic program. Here, we investigate the
154 molecular interactions and transcriptional co-regulation on a shared regulatory program of NR2F2 and
155 SOX18. Analysis of a publicly available single-cell RNA sequencing (scRNA-seq) dataset of hESCs to
156 arterial or venous ECs differentiation[42], as well as a scRNA-seq atlas of mouse embryos at E8.5,[44]
157 identifies a subset of the venous population that co-expresses both NR2F2 and SOX18 (**Supp Fig. 1A-**
158 **B**). We also observed co-expression in EC from vascular anomaly specimens, including infantile
159 hemangioma (IH), venous malformations (VM), and arteriovenous malformations (AVMs) (**Supp Fig.**
160 **1C-E**). These observations prompted us to investigate how potential direct protein-protein interactions
161 (PPI) between NR2F2 and SOX18[45] might influence the regulation of common transcriptional targets,
162 and how such interactions may contribute to both physiological and pathological vascular states.
163
164 To explore a possible direct protein interaction between these two TFs, we modelled the SOX18/NR2F2
165 heterodimer using Alphafold 3 (**Supp Fig. 1F,** pLDDT = 51.1, pTM = 0.363, and ipTM = 0.145) [46,47].
166 The predicted structure revealed a binding interface between the DNA-binding domain (DBD) of
167 NR2F2 (amino acids 95-97) and the central transactivation domain (TAD) of SOX18 (amino acids 226-
168 235) (**Supp Fig. 1F**). The model suggests that SOX18 might inhibit by NR2F2 and that NR2F2 might
169 influence SOX18 PPIs with other factors since its TAD domain is used to interact with other proteins.
170
171 To functionally validate the modelled predictions, we used a combination of quantitative molecular
172 imaging approaches to assess PPI (Number and & Brightness (N&B)), protein-chromatin interactions
173 (Single Molecule Tracking (SMT)), and protein co-diffusion in living cells at single-molecule
174 resolution (Cross raster image correlation spectroscopy (cRICS))[48]. cRICS measures the co-diffusion
175 of two proteins and N&B measures the oligomeric state of the proteins, enabling the measurement of
176 PPIs in real-time. By contrast, SMT measures the mobility and proportion of diffusing proteins, as well
177 as their temporal occupancy[49–52] (**Supp Fig. 2**).
178
179 This combination of assays was performed using $NR2F2^{WT}$-halotag in the presence of SOX18 or the
180 reciprocal condition, SOX18-halotag in the presence of $NR2F2^{WT}$. SMT showed that when both TFs
181 are together in the same nucleus, there is a significant change in the proportion of the TF population
182 that interacts with the chromatin. When imaging $NR2F2^{WT}$ in the presence of dark SOX18, the nuclear
183 receptor exhibits more diffusive behaviour compared to when it is expressed alone (**Fig. 1A–B**). In
184 contrast, SOX18 displays reduced mobility in the presence of dark $NR2F2^{WT}$, compared to its behaviour

185 in the absence of NR2F2^{WT} (**Fig. 1C-D**). These changes in mobility observed by SMT support a model
186 in which SOX18 inhibits the ability of NR2F2 to stall on DNA while NR2F2 has the opposite effect on
187 SOX18 stimulating its binding to DNA. Furthermore, cRICS and N&B analysis reveal a reduction in
188 both homo-dimer formation and co-diffusion of NR2F2 homo-dimers in the presence of SOX18 (**Fig.**
189 **1E-F**). This further supports a direct interaction between the SOX18 and NR2F2 TFs and a dynamic
190 competition model, whereby these two TFs antagonistically regulate access to shared genomic loci or
191 chromatin territories. Collectively, these observations describe how protein-partners can influence each
192 other's biophysical behaviours (summarized in **Table 1**). Characterizing this interplay prompted us to
193 explore whether these TFs may differentially modulate a shared gene regulatory program in endothelial
194 cells.
195
196 **NR2F2 and SOX18 antagonistically regulate a subset of genes of the arteriovenous program**
197 To explore a potential antagonistic modulation of genes between NR2F2 and SOX18, we integrated
198 two previously published RNA-seq datasets, comparing known EC identity genes. The first column
199 examines HUVECs with NR2F2 deletion (KO) and the second dataset examines HUVECs with SOX18
200 inhibition (treated with a small molecule inhibitor, SM4[15,18] (**Supp Fig. 3A**). We observed that the gene
201 response to the perturbed activity of one TF consistently leads to an opposite response when the other
202 TF is perturbed. This antagonistic response for a subset of specific arteriovenous markers prompted us
203 to expand our analysis to a larger gene set.
204
205 To determine common target genes for these two TFs on a genome-wide scale, we combined four
206 publicly available sequencing datasets. We layered NR2F2 and SOX18 chromatin immunoprecipitation
207 sequencing (ChIP-seq) data sets[15,48] with ChiP-seq datasets for marks of active gene expression (e.g.
208 H3K27ac and H3Ke4me3 ENCODE consortium[53]) and intersected these peaks with assay for
209 transposase-accessible chromatin (ATAC-seq) results from HUVECs that were either untreated or
210 treated with SOX18 inhibitor, SM4[18,32]. This approach enabled us to identify regulatory regions that are
211 co-bound by SOX18 and NR2F2 and that change their accessibility upon SOX18 inhibition. We
212 identified 139 regions with an enhancer-like signature (ENCODE cCRE[53] and H3K27ac, **Supp Fig. 3B**,
213 yellow bar and light blue track) that are recruited by SOX18 and NR2F2 and less accessible upon SM4
214 treatment (**Supp Fig. 3B**, green bar). Peak to gene analysis[54,55], assigned these enhancers to probable
215 transcription start sites (TSS) and revealed 245 putative target genes (**Supp Table 1**). Cross checking
216 known markers from that reference gene list, with a publicly available scRNA-seq dataset of hESC to
217 endothelial differentiation[42], reveals that both SOX18 and NR2F2 potentially co-regulate the arterio-
218 venous program – i.e. regulate genes enriched in either artery or vein ECs (**Supp Fig. 3B**) and narrowed
219 down the list of candidate genes to 70 genes with an arterial or venous specific expression profile (**Supp**
220 **Table 2**). This observation suggests that SOX18 might alter chromatin availability in a way that

221 disfavours NR2F2 co-binding, hence explaining the change in protein diffusion previously observed
222 with SMT **(Fig. 1A-D)**.
223
224 To further validate SOX18-dependency of these 70 target genes, we performed qPCR analysis on
225 HUVECs treated with SM4 (**Fig. 2A**). This approach revealed that these genes are either trans-activated
226 or repressed by SOX18. We then assessed whether a subset of these genes is co-regulated by both
227 NR2F2 and SOX18. A random subset of these 70 genes (**Fig. 2A**, yellow highlights) was selected for
228 further investigation. For example, at the DCBLD2 locus, overlaying ChIP-seq and ATAC-seq datasets
229 revealed two binding sites that correspond to both NR2F2 and SOX18 (ChIP-seq in HUVECs, black
230 boxes). These regions both show a change in chromatin accessibility upon SM4 treatment (ATAC-seq
231 of HUVECs treated with SM4, purple tracks) and are annotated as candidate cis-regulatory elements
232 (cCREs, yellow boxes), indicating enhancer-like function. These results show that SOX18 and NR2F2
233 bind overlapping enhancer regions, and that SOX18 inhibition alters chromatin accessibility at these
234 sites (**Fig. 2B**, green boxes).
235
236 We then compared the random gene subset to a publicly available scRNA-seq dataset to hESC-to-
237 endothelial cell differentiation, revealing an expression pattern for genes associated with an arterial
238 phenotype (**Fig. 2C**, blue box). This suggests that disruption of SOX18/NR2F2 co-regulation has the
239 potential to impact EC identity by dysregulation of artery enriched genes. To test this, we performed
240 qPCR on HUVECs treated with either DMSO as a control, or the NR2F2 inhibitor CIA1[56] alone or in
241 combination with SM4. A striking feature of the gene expression profiles under different treatments
242 was a clear opposite response to either NR2F2 inhibition or the simultaneous blocking of both TFs.
243 When cells were treated in the presence of both inhibitors, there was a consistent pharmacological
244 rescue by SOX18 inhibitors on CIA1 dysregulated targets (**Fig. 2D**, **Supp Fig. 3C**). These observations
245 strongly suggest that NR2F2 and SOX18 jointly regulate a subset of shared direct target genes in an
246 antagonistic manner, which plays a role in endothelial cell identity.
247
248 This mechanistic insight raised the question of whether disrupting the cooperative antagonism of these
249 TFs during development may underlie human vascular anomalies. A rare vascular phenotype in a
250 paediatric proband harbouring a novel NR2F2 mutation provided an opportunity to test this hypothesis.
251
252 **A *de novo* NR2F2 variant is identified in a novel vascular anomaly**
253 In 2020, a five-year-old proband was diagnosed with multiple vascular lesions that radically impacted
254 development and quality of life. Owing to the rarity and severity of the disease and its resistance to
255 treatment, whole-exome sequencing (WES) was performed. WES identified a heterozygous VUS in
256 exon 3/3 of the NR2F2 gene (c.994del (G), p.Ala332Pro). A review of the Online Mendelian Inheritance
257 in Man (OMIM) entry for NR2F2 identified *epicanthus inversus* (a distinctive eyelid fold abnormality)

258 as one of its clinical features, which is a relatively uncommon condition and was also observed in this
259 proband. This prompted us to focus our analysis further on this NR2F2 variant.
260
261 The identified mutation (NM_021005.4), Chr15 (GRCh38): g.96337371del, introduces a frame-shift
262 beginning at amino acid position 332, resulting in an alanine-to-proline substitution leading to a
263 scramble and truncation of the ligand binding domain (LBD) (**Fig. 3A**). The c994del variant
264 ($NR2F2^{c994del}$, hereafter $NR2F2^{Mut}$) has not been reported previously, making it clinically novel.
265 Previous NR2F2 deleterious variants have been identified and shown to cause a wide range of
266 symptoms, ranging from cardiac to sex determination defects[9–11,13], unlike this VUS, which seems to be
267 involved explicitly with severe vascular defects.
268
269 To investigate the potential molecular consequences of this mutation, we used AlphaFold 3 [46,47] to
270 perform *in silico* modelling and examine how the frameshift mutation affects the LBD conformation.
271 Structural predictions of the $NR2F2^{WT}$ LBD determined that this region is critical for its homo-
272 dimerization[57]. In contrast, the $NR2F2^{Mut}$ confirmation showed significant deviation, with a loss of α-
273 helical structures following amino acid 332. This suggests that the mutation causes an abnormal folding
274 confirmation compared to the $NR2F2^{WT}$ LBD, starting after amino acid 332 (**Fig. 3B**, **Supp Fig 4A**).
275
276 WES also detected a hemizygous variant in MAP7D3 (c.1783dupA, p.Met580Asnfs*4). The variant is
277 found in exon 10/19 of MAP7D3 gene (NM_024597.4), ChrX (GRCh38): g.136230397dup, which
278 causes a frameshift and is expected to result in a nonsense mediated mRNA decay. This variant has
279 been found in other individuals and is not considered a ClinVar variant on gnomAD (Genome
280 Aggregation Database (gnomAD) v 4.1.0). The MAP7D3 gene has not been reported as a key regulator
281 of vascular development, and there is no literature on the role of this factor in the endothelium.
282 Therefore, we focused our investigation on the cell-autonomous role of NR2F2 dysfunction, given its
283 well established role in venous EC identity during embryogenesis.
284
285 We started by investigating the expression profiles of NR2F2 and SOX18 in a human embryo at CS17
286 (gestational age: 42-44 days). During physiological vascular development, immunofluorescence
287 staining revealed that ECs co-expressing both TFs can be found in the liver, gut, aorta, and at the
288 junction of the cardinal vein (**Supp Fig. 4B**). Examination of the proband's liver and duodenum (polyp)
289 tissue samples revealed co-expression of NR2F2 and SOX18 in CD31-positive vessels (**Supp Fig. 4C-**
290 **D**). Two subsets of vessels were observed: one that only expresses SOX18 (most likely arteries based
291 on their morphological features) and the other co-expresses both NR2F2 and SOX18 (most likely veins
292 based on the expression of NR2F2 and morphological features) **(Supp Fig. 4C-D**).
293

294 Early indications of the disease manifested as recurrent gastrointestinal haemorrhages, commencing
295 when the patient was a newborn. Other clinical features of the disease became apparent as the proband
296 developed. These include multiple gastric and small bowel mucosal vascular lesions characterized by
297 an increased number of ectopic vessels and dilated capillaries, non-cirrhotic portal hypertension
298 associated with hepatofugal flow, and diffuse hepatic arterioportal blood shunting that did not respond
299 to surgical shunt treatments (**Fig. 3C-D**). Due to chronic gastrointestinal haemorrhages, a porta-cath
300 was necessary for regular blood and iron transfusions, and plans were underway to list for a liver
301 transplantation by pre-school age.
302
303 Mutations in key developmental TFs specific to EC development have been reported to cause rare
304 vascular diseases[60,61]. For instance, mutations in the transactivation domain of SOX18 TF are known
305 causes of HLTRS, which has a dominant-negative effect and suppresses the endogenous function of the
306 wild-type protein[48,62,63]. Remarkably, the FDA-approved drug propranolol has shown considerable
307 efficacy in enhancing the clinical management of the HLTRS syndrome[31]. Since the early 2010s, this
308 drug has been primarily used as the first-line treatment for IH, the most common vascular tumor, whose
309 mechanism of action also relies on SOX18 inhibitory activity[30,31,33]. Given propranolol's established
310 safety for use in paediatric vascular disorders, the identification of its recent mode of action via SOX18
311 blockade, and the worsening condition of the proband with limited therapeutic options, a decision was
312 made to use propranolol to manage the proband's condition.
313
314 **Treatment and recovery**
315 Propranolol treatment was initiated at a dose of 1.5mg/ml/kg in August 2021. By December 2021,
316 haemorrhaging had resolved, and haemoglobin levels stabilized, resulting in the patient no longer
317 requiring transfusions (**Fig. 3E**). In early 2023, a Doppler ultrasound was performed, and it determined
318 that hepatopetal flow had been restored (**Fig. 3F**). Due to the proband no longer requiring transfusions
319 the porta-cath was removed, and the liver transplant was cancelled. At the time of writing this
320 manuscript the treatment has been a success, with the probands' quality of life drastically improving,
321 allowing for a return to a more normal and fulfilling life (**Fig. 3G**). Following the successful treatment,
322 we aimed to unravel the underlying cellular and molecular mechanisms of propranolol's therapeutic
323 effect. Importantly, the co-expression of SOX18 and NR2F2 in the proband's endothelium **(Supp Fig.**
324 **4C-D**) raises the question whether NR2F2 mutation would directly affect the interplay with SOX18 and
325 impact their co-regulation process and whether propranolol treatment has the potential to restore this
326 imbalanced relationship.
327
328 **NR2F2^{Mut} impairs venous but not arterial differentiation**

329 We started by investigating the pathogenicity of the NR2F2 variant. Given its importance for vein
330 identity in model organisms, we tested the impact of the variant on vein EC differentiation in a highly
331 efficient human stem cell to venous and arterial EC differentiation model[42] (**Fig. 4A**). We generated
332 H1-hESC lines containing the proband-specific variant in a homozygous fashion (**Fig. 4A**, **Supp Fig.**
333 **5A-D**). Western blotting confirmed that the $NR2F2^{Mut}$ lines had NR2F2 proteins at comparable
334 expression to wild type, but, as expected, at a lower molecular weight (predicted $NR2F2^{WT}$ = 45.5kDa
335 (414AA) and $NR2F2^{c994del}$ = 41.03kDa (377 AA), consistent with a premature stop codon. (**Supp Fig.**
336 **5C**).
337
338 To assess the phenotypic impact of the NR2F2 variant and its cell autonomous role, we differentiated
339 wild type control and $NR2F2^{Mut}$ hESCs into vein and artery ECs. The differentiation assay utilized
340 FACS and qPCR readouts to assess cellular and molecular levels of arterial and venous differentiation
341 markers (vein=CD73, *APLNR*, *NRP2,* and SOXFs). In line with its known role as a hallmark of venous
342 identity, $NR2F2^{Mut}$ caused an increase in the overall number of ECs (**Fig. 4B**) and resulted in a
343 significantly decreased levels of the hESC-derived vein marker CD73 (**Fig. 4C**, CD73+ ECs, **Supp Fig.**
344 **5D**). The additional venous markers, *APLNR, EPHB4, NRP2*, and *NT5E* (*CD73*) were also down as
345 measured by qPCR, further expanding FACS observations and indicating a potential defect in achieving
346 full venous identity (**Fig. 4D**). NR2F2 deficiency also did not change the expression of SOX18 or other
347 SOXF's (**Fig. 4E)**. The lack of change in the SOX7 and SOX18 expression in the NR2F2 variant clones
348 suggested that this TF is not directly upstream of SOXF members in the model of venous differentiation
349 (**Fig 4E**). In contrast to its effect on vein endothelial cells, $NR2F2^{Mut}$ did not influence the arterial
350 differentiation process (**Fig. 4F**). Of interest is the finding that $NR2F2^{Mut}$ cells make more ECs because
351 it aligns with the patient duodenum tissue sample showing an increased number of ectopic, thin-walled
352 vessels (**Fig. 3C**). These findings show that the $NR2F2^{Mut}$ can autonomously interfere with EC subtype
353 transcriptional profiles, specifically within the venous compartment. Based on the previous interplay
354 between SOX18 and NR2F2 under physiological conditions, we next set out to determine the mode of
355 action of the proband's mutation.
356
357 **Molecular mechanism of $NR2F2^{Mut}$ impaired function**
358 Because the proband is heterozygous and has both wild type and variant alleles expressed, we modelled
359 the effect of this abnormal configuration on homodimer formation. Crystal structure studies of the LBD
360 of $NR2F2^{WT}$ further confirmed the dimerization residues involve several α-helices, including 7 (amino
361 acids 297-301), 8 (amino acid 378), 9 (amino acids 335 and 339), and 10 (amino acids 358-372), along
362 with the loop between α-helices 8 and 9 (amino acids 323 and 324)[57]. Because the location of the frame-
363 shift in the variant occurs at amino acid 332, these dimer residues are lost, potentially resulting in an
364 abnormal folding conformation at the C-terminus. As expected, the *in silico* modelling indicates that
365 the loss of dimer residues results in the inability of the variant and WT to form a dimer. The mutation

366 results in a disordered conformation, which likely creates an unstable interface compared to NR2F2^{WT}
367 (**Fig. 5A**, **Supp Fig 6A-C**), which could result in a global destabilization of the NR2F2 homodimer
368 pool.
369
370 Consistent with the observed model, cRICS and N&B imaging showed the NR2F2^{Mut} almost completely
371 lost its ability to co-diffuse and form homo-dimers (**Fig. 5B-C**). Following on, we next investigated
372 how the loss of homo-dimerization affects the variant's ability to navigate and interact within the
373 nuclear environment. SMT imaging determined that most of the variant population has an increased
374 diffusion profile compared to its WT counterpart (**Fig. 5D-E** (HeLa), **Supp Fig. 6D-E** (HUVEC)).
375 Taken together, the data indicate that the variant is unable to homo-dimerize, allowing the vast majority
376 of NR2F2^{Mut} molecules to diffuse as monomers, hence dramatically impacting the total pool of NR2F2
377 available to perform its function.
378
379 We next assessed whether homo-dimerization is necessary for NR2F2 to bind and interact with its
380 environment. Temporal occupancy SMT established that the variant spends less time searching for
381 binding sites as indicated by duration of short dwell times (**Supp Fig. 6F**), but a similar amount of time
382 interacting when an interaction occurs as indicated by duration of longer dwell times (**Supp Fig. 6G**).
383 Additionally, the variant has a much smaller proportion of the population bound at any time indicated
384 by the reduction in the ratio of long to short dwell time events (**Supp Fig. 6H**). These results
385 demonstrate that the variant causes interactions to be less stable through the loss of target gene search
386 pattern and fewer of the population undergoing longer specific interactions with the chromatin
387 (summary of the variant biophysical features in **Table 2**).
388
389 The biophysical characterization of the defects establishes that the NR2F2^{Mut} severely disables NR2F2
390 activity and interferes with its physiological and molecular function, leading us to define the variant as
391 a loss-of-function variant. We next questioned whether the variant also impacts NR2F2's capacity to
392 hetero-dimerize with a known protein partner. Previous studies have shown direct interaction of NR2F2
393 and SOX18 in cell-based assays[18,48], and it is known that these two TFs together induce *Prox1*
394 expression in the venous endothelium to specify lymphatic endothelial cells[19]. However, this is a
395 synergistic relationship, and our data suggests an antagonistic interaction with respect to gene induction
396 **(Fig. 2D)**
397
398 To determine if NR2F2^{Mut} also lost its ability to interact with SOX18 we performed cRICS, N&B, and
399 SMT on either NR2F2^{WT} or NR2F2^{Mut}-halotag in the presence of SOX18 or the reciprocal condition.
400 cRICS and N&B analysis of NR2F2, discussed above, identified a loss of co-diffusion and homo-dimer
401 formation for NR2F2^{Mut} (**Fig. 5B-C**). The same trend was also observed for NR2F2^{Mut} in the presence
402 of SOX18 (**Fig. 5F-G**). To understand how hetero-dimerization affects the diffusion profile of both

403 TFs, we turned to SMT. This approach revealed when NR2F2^{WT} is present SOX18 mobility becomes
404 more confined, whereas when NR2F2^{Mut} is present there is a negligible change in SOX18 mobility (**Fig.**
405 **5H-I**). By contrast, NR2F2^{Mut} mobility remains unchanged regardless of SOX18 presence (**Fig. 5J-K**).
406 Taken together, the observations suggest NR2F2^{Mut} most likely influences SOX18 mobility indirectly
407 through the interference with its wild-type counterpart (summary of NR2F2/SOX18 interplay in **Table**
408 **2**).
409
410 Collectively, these findings reveal that NR2F2^{Mut} is a severe loss-of-function mutation that disrupts both
411 homo-and hetero-dimer formation, leading to a deficiency of NR2F2. The frameshift mutation results
412 in a disordered and destabilized LBD, which depletes the homo-dimer pool. Importantly, NR2F2^{Mut} also
413 fails to interact productively with SOX18, suggesting that the variant may interfere with other key
414 regulators of venous identity, akin to the mechanism reported for the SOX18 dominant-negative
415 mutation[48]. These mechanistic disruptions likely underlie the endothelial phenotype observed in the
416 proband, supporting a model in which balanced NR2F2-SOX18 interactions are essential for endothelial
417 transcriptional programs and venous homeostasis. These findings prompted us to question whether the
418 proband's recovery following propranolol treatment may have occurred, at least in part, through a
419 rescue mechanism that involves the pharmacological blockade of SOX18 activity.
420
421 **Drug repurposing and molecular mechanisms of treatment**
422 Recent findings have demonstrated that both propranolol and a small molecule inhibitor of SOX18,
423 SM4 inhibit the differentiation of hemangioma stem cells into hemangioma endothelial cells in a
424 SOX18-dependent manner[30,31,33,64] and also blocks SOX18 pioneering function during virus-induced
425 LEC reprogramming in Kaposi's sarcoma[65]. Specifically, propranolol is composed of a R(+) and S(-)
426 enantiomer mixture at a 1:1 equimolar ratio, with the R(+) enantiomer (R(+)propranolol) devoid of
427 beta-adrenergic effects.
428
429 Previous research has demonstrated that the R(+) enantiomer is capable of disrupting SOX18 activity
430 [30,31,66,67]. Given that NR2F2 and SOX18 are co-expressed in a subset of the venous endothelium and
431 antagonistically co-regulate a common set of arterial-related genes, we sought to determine whether
432 R(+)propranolol-induced SOX18 inhibition has the potential to rescue NR2F2 loss-of-function caused
433 by the variant NR2F2^{Mut}.
434
435 Taking advantage of molecular imaging, we first evaluated if R(+)propranolol directly engages with
436 NR2F2 by measuring its molecular mobility and temporal interaction times using SMT and N&B.
437 Collectively, these experiments indicate that R(+)propranolol (Rprop) does not interact with or effect
438 NR2F2 protein since it does not disrupt a broad range of key biophysical behaviours (**Fig 6A-B, Supp**
439 **Fig 7 A-D**). Because R(+)propranolol does not disrupt NR2F2, we hypothesized that the treatment of

440 the proband would have to be through the inhibition of SOX18. To test this hypothesis, we next
441 examined the effects of this compound on NR2F2-SOX18 interactions using SMT, N&B, and cRICS.
442 In the absence of the drug, SMT imaging revealed that the presence of SOX18 increases the proportion
443 of diffusing $NR2F2^{WT}$ molecules compared to $NR2F2^{WT}$ alone, suggesting that SOX18 is directly or
444 indirectly disfavoring NR2F2 interaction with the chromatin. Additionally, when SOX18 activity is
445 disrupted by R(+)propranolol, we observed a decrease in the proportion of diffusing $NR2F2^{WT}$
446 molecules, indicating that interference of R(+)propranolol with SOX18 restores the chromatin-bound
447 fraction of $NR2F2^{WT}$ to its baseline state (**Fig. 6C-D**). Conversely, there is little change in $NR2F2^{Mut}$
448 diffusion profile in the presence of SOX18 with or without R(+)propranolol (**Fig. 6E-F**). This suggests
449 that the protective effect of R(+)propranolol is mediated at a molecular level, specifically by indirectly
450 modulating the availability of the $NR2F2^{WT}$ pool through an interference with SOX18 activity. In other
451 words, this work builds on previous findings that inhibition of SOX18 by pharmacological blockade
452 reduces NR2F2 and SOX18 interaction[32] and establishes that SOX18 inhibition favours an increase of
453 $NR2F2^{WT}$ activity on the chromatin (summary of drug mode of action, **Table 3**). Having elucidated that
454 R(+)propranolol-induced SOX18 inhibition restores a vast proportion of the $NR2F2^{WT}$ behaviour, we
455 next investigated whether R(+)propranolol is able to rescue the venous phenotype caused by the NR2F2
456 variant in a human pre-clinical model of stem cell to venous endothelial cell differentiation.
457
458 **R(+)propranolol effects are endothelial cell autonomous and rescues venous defects caused by**
459 **$NR2F2^{Mut}$**
460 To perform an orthogonal validation of data obtained from single-molecule imaging, we next employed
461 the hESC to venous EC differentiation assay. The experimental design relies on a differentiation
462 protocol in the presence or absence of SOX18 blockers (either SM4 or R(+)propranolol) when cells
463 transition from vein intermediates (D3) to vein (D4). (**Fig. 7A**). To assess whether the SOX18 inhibitor
464 exert an effect on $NR2F2^{Mut}$-induced venous defects, we analyzed the three independent clones with the
465 proband mutation (**Supp Fig. 5D**). These clones were evaluated for CD73 expression by FACs and
466 venous marker expression by qPCR (**Fig. 7B-D**). Treatment with SOX18 inhibitors significantly
467 restored CD73 expression in $NR2F2^{Mut}$ cells relative to DMSO-treated cells while having no effect on
468 physiological CD73 expression in $NR2F2^{WT}$ (**Fig. 7B**, **C**). Similarly, expression of classic venous
469 markers *APLNR, NRP2, and EPHB4*, along with three additional markers previously identified
470 (*FAM171A, GALNT1,* and *MBNL2*) was also rescued following R(+)propranolol treatment (**Fig. 7D**).
471 Molecular rescue was consistent for all clones tested with no significant variability in response to the
472 inhibitors (**Supp Fig. 7E-G**) These results established that the recovery of the venous differentiation
473 defects caused by NR2F2 variant is meditated through SOX18 blockade. The validation with this cell-
474 based assay determined that the R(+)propranolol molecular mechanism specifically acts on the venous
475 endothelium in a cell autonomous manned and suggests that SOX18 inhibition in the proband has
476 contributed to a restored physiological function of the venous vasculature.
477

478 **Discussion**

479 *The NR2F2-SOX18 axis as a regulatory hub in endothelial identity*

480 This study centers on the hypothesis that NR2F2 and SOX18 function cooperatively to regulate venous
481 identity and the fate of endothelial cells. Here, we show that during physiological venous differentiation,
482 SOX18 and NR2F2 establish a regulatory equilibrium, dynamically influencing each other's chromatin
483 binding and transcriptional activity. Previous genetic studies have shown that these synergistic
484 pathways regulate PROX1 and lead to the development of lymphatic endothelial cells, however the
485 dynamics of this coordination at a biophysical and biochemical levels have remained uncharacterized.
486 The discovery of a *de novo* NR2F2 mutation in a proband that results in severe vascular defects
487 presented a unique opportunity to examine what happens when the equilibrium between NR2F2 and
488 SOX18 becomes unbalanced. The proband's improvement after the start of propranolol treatment,
489 including cessation of hemorrhaging and the return of hepatofugal flow in the portal vein, strongly
490 supports a model in which SOX18 inhibition compensates for NR2F2 dysfunction. *In silico* and live-
491 cell imaging revealed that the $NR2F2^{Mut}$ protein is unable to form homo-dimers and cannot stably
492 interact with SOX18, resulting in the disruption of gene regulation. The loss of NR2F2 and SOX18
493 interactions was found to be a key driver of the proband's vascular pathology, implicating the loss of
494 NR2F2-SOX18 coordination as a significant contributor to this disease. Given the antagonistic
495 transcriptional relationship between NR2F2 and SOX18, we hypothesized that inhibiting SOX18 might
496 rebalance transcriptional regulation.

497

498 *An updated molecular mechanism for investigating TFs*

499 Based on this study, we propose a molecular model explaining how Propranolol treatment benefited the
500 proband. Under normal circumstances, a physiological balance between NR2F2 and SOX18 ensures
501 the coordinated transcriptional regulation of common target genes central to arteriovenous identity.
502 However, in the proband's case, a heterozygous variant in NR2F2 causes only half of the pool of NR2F2
503 molecules to function properly, leading to a shift in balance in favour of SOX18 activity. This results
504 in transcriptional dysregulation being over-dominated by SOX18. To correct this imbalance, a
505 molecular strategy based on SOX18 inhibition is used to compensate for the larger pool of SOX18
506 compared to functional NR2F2 and to restore a relative equilibrium between the remaining functional
507 NR2F2 and less active SOX18 molecules (**Fig. 7E**). Our findings introduce a novel concept to correct
508 loss-of-function mutations of transcriptional regulators by targeting TFs interplay, ultimately
509 normalizing co-regulated genes to a physiological level.

510

511 *Using molecular imaging to investigate pharmacological on-target engagement*

512 Targeting TFs to modulate gene expression has been studied for decades. Historically, TFs have been
513 considered "undruggable" due to their intrinsic disordered domains, lack of a traditional drug binding

514 pocket, and dynamic nature[68]. This study highlights the potential of using quantitative molecular
515 imaging as a strategy to perform on-target engagement. Using SMT has unlocked the ability to assess
516 a molecular target in the presence of its inhibitor[69,70]. Here, we firmly establish that the R(+)propranolol
517 mode of interference is mediated via SOX18 disruption, whereas NR2F2 behavior remains unaffected
518 by this drug. Molecular imaging thus provides a powerful tool to evaluate the interaction between drugs
519 and molecular targets, offering a direct method to validate therapies aimed at specific pathways.
520
521 *A new therapeutic pathway for congenital vascular malformations*
522 More broadly, vascular anomalies have been linked to alterations in signaling pathways associated with
523 the development of AVMs, cutaneous-mucosal venous malformations, and capillary malformations
524 with AVM[71]. Specific signaling components are crucial for EC identity, including NOTCH, a key
525 marker of arterial differentiation. Notably, the loss of signaling from either NOTCH or platelet-derived
526 growth factor subunit B (PDGFB), has been associated with the formation of AVMs[72,73]. Additionally,
527 SOX18 has been shown to regulate NOTCH1[74,75], while the deletion of NR2F2 in HUVECs has been
528 found to alter the expression of NOTCH2-4 and decrease PDGFB expression[15,73]. Collectively, these
529 findings suggest that the NR2F2 and SOX18 signaling axis might be essential for regulating pathways
530 implicated in vascular malformations. This study explores the potential of exploiting the NR2F2-
531 SOX18 antagonistic relationship as a novel therapeutic target for treating vascular malformations.
532
533 The findings from this work establish a clear window of opportunity for therapeutic intervention in the
534 context of congenital malformations acquired during fetal development. Vascular malformations
535 present a unique challenge due to their complexity and location in the body, often rendering surgical
536 intervention impractical[76]. In such cases, pharmacological therapies are the preferred option. An
537 example is sirolimus (rapamycin), an mTOR inhibitor, which has shown positive results in some
538 patients[77,78]. However, due to the heterogeneity of the disease, not all individuals respond to this therapy,
539 highlighting the need for alternative pharmacological options[79]. This study suggests that blood
540 vasculature plasticity during postnatal organogenesis, which relies on developmental pathways, can be
541 leveraged to treat VUS. Here, we uncover that the balanced activity of SOX18 and NR2F2 is essential
542 for the proper development of arteriovenous identity, providing new insights into the molecular
543 mechanisms underlying vascular malformations and new pathways that may be exploited for future
544 therapies.
545
546 In summary, this work offers a model of how paired molecular switches exert a balanced cooperative
547 and competitive behaviour to instruct vascular development. By combining quantitative molecular
548 imaging with patient-derived insights, we establish a framework for investigating other rare disorders
549 in the context of transcription factors uncoupling.
550

551 **Methods and Materials**

552 **Cell culture**
553 Hela cells were cultured in supplemented DMEM (Gibco) with 10% FBS, 1% GlutaMAX (Gibco), 1%
554 MEM Non-essential amino acids (MEM NEAA, Gibco). Cells were cultured at 37°C with 5% CO_2.
555 HUVEC cells were cultured in EBM-2 media (Lonza) supplemented with EGM-2 bullet kit (Lonza).
556 Cells were cultured at 37 °C with 5% CO_2.
557
558 **hESC**
559 Undifferentiated H1-hESC (Wicell, WA01) were maintained in mTeSR™ plus medium (StemCell
560 Technologies, #100-0276,100-1130) in monolayer culture on Geltrex (ThermoFischer Scientific, #
561 A1413302). The medium was changed on alternate days per the manufacturer's guidelines. The cells
562 were split and maintained according to a previously published protocol[80].
563
564 **Generation of H1-hESC with NR2F2^{c994del} mutation**
565 H1-hESC containing NR2F2^{c994del} mutations were generated using CRISPR-Cas9 cells with synthetic
566 gRNA (Synthego), Cas9 (Alt-R™ S.p. HiFi Cas9 Nuclease V3, IDT, #1081060) and HDR donor
567 template (IDT). The knock-in strategy, gRNA sequence, and HDR oligo sequence are shown in
568 **Supplementary Figure 1C**.
569
570 H1-hESCs at 40-50% were treated with 10 μM ROCK inhibitor (Thiazovivin; Tocris, #3845) 24h
571 before the electroporation. Cells were then dissociated using Accutase, followed by dilution in
572 DMEM/F12 (1:5) and centrifugation at 300g for 5 mins. Subsequently, cell pellets were resuspended in
573 PBS and centrifuged at 300g for 5 mins. 200,000 cell pellets were then resuspended in 10 μl Buffer R
574 (for each well in 24 wells plate). Cas9-gRNA complex was prepared by mixing 36μM Cas9 (final
575 concentration) and 0.5 μl gRNA and incubated for 20 mins at RT. HDR donor oligo was added to the
576 mix, followed by H1-hESC. Cells were electroporated using the NeonTransfection system (Fischer
577 Scientific, Invitrogen™ #MPK5000) according to manufacturer guidelines (electroporation condition:
578 1400V, 20ms pulse width, 1 pulse). Following electroporation, cells were transferred to the Geltrex-
579 coated 24-well plate containing 500 μl mTeSR plus + 10 μM Thiazovivin. The medium was changed
580 to 24 hours post-transfection, followed by DMEM/F12 wash, and switched to mTeSR plus medium.
581 Single cells were then FACS sorted (MA900), expanded, and Sanger sequenced to identify clones
582 containing NR2F2^{c994del} mutation.
583
584 **Differentiation of H1-hESC to Artery and vein Endothelial cells**
585 The protocol for differentiating artery and vein endothelial cells from H1-hESC has been published[42,80].
586 In short, at day 0, H1-hESCs were dissociated into single cells with Accutase (Sigma, A6964), and
587 175,000 cells were plated in each well of 12 wells of cell culture plates pre-treated with geltrex for 1h
588 at 37°C. Cells were seeded in mTeSR plus + 1μM Thiazovivin (Tocris, #3845). On day 1, cells were
589 washed briefly with DMEM/F12 (Thermo Fischer Scientific, 11320082) and differentiated in a
590 primitive streak induction medium. On Day 2, cells were briefly washed and then differentiated in a
591 lateral mesoderm induction medium (Day 2, lateral mesoderm). For Artery differentiation, cells were
592 briefly washed and differentiated in an Artery induction medium for 24 h. For Veins, the Day 2 lateral
593 mesoderm induction medium was incubated in day 3 vein intermediate medium, followed by day 4 vein
594 medium.
595

Day 1: Mid primitive streak induction	Final	Stock
Activin A	30 ng/mL	50ug/ml
BMP4	40 ng/mL	100ug/ml
CHIR99021	6 µM	10mM (10mg/2.15ml)
FGF2	20 ng/mL	100ug/ml

Day 2: Lateral mesoderm	Final	Initial
BMP4	40 ng/mL	100ug/ml
GDC0941	2.5µM	10mM
VEGF	100 ng/mL	100ug/ml
XAV939	1 µM	10mM
Forskolin	10 µM	10mM
SB505124	2 µM	10mM
AA2P	200 µg/mL	50mg/ml

Day 3; ARTERY meidum		
Activin A	15 ng/mL	50ug/ml
GDC0941	2.5 µM	10mM
VEGF	100 ng/mL	100ug/ml
XAV939	1 µM	10mM
AA2P	200 µg/mL	50mg/ml
DMH1	250nM	1mM

Day 3,4: VEIN medium		
Day 3 Vein medium	**Final**	**Initial**
SB505124	2 µM	10mM
DMH1	250nM	1mM
RO4929097	2 µM	10mM
VEGF	100 ng/mL	100ug/ml
XAV939	1 µM	10mM
AA2P	200 µg/mL	50mg/ml
Day 4 Vein medium	**Final**	**Initial**
SB505124	2 µM	10mM
RO4929097	2 µM	10mM
PD0325901	0.5 µM	5mM
CHIR99021	1 µM	10mM
AA2P	200 µg/mL	50mg/ml

596
597
598 **Rescue experiment of vein endothelial cells using R(+) Propranolol and Sm4:**
599 For rescue experiments, NR2F2^{WT} and NR2F2^{c994del} were treated with R(+) propranolol at 15 µM and
600 Sm4 at 30 µM while differentiating cells in a day 4 vein medium, and cells were processed for FACS
601 and qPCR analysis as described in the respective sections.
602
603 **Flow Cytometry**
604 Cells were dissociated by incubation in Accutase for 5 mins at 37 ˚C. Dissociated cells were diluted 1:5
605 in DMEM/F12+5% FBS (Thermo Fischer Scientific, # A5670401) and centrifuged at 350g for 5
606 minutes. Cell pellets were resuspended in FACS buffer (PBS+1mM EDTA+2% FBS+1%

607 penicillin/Streptomycin). Cells were then blocked for 5 minutes in the presence of an FcR blocking
608 reagent (Miltenyi Biotec, #130-059-901), followed by staining with PE anti-human CD73 (BioLegend,
609 #344004) and FITC anti-human CD144 (BD Biosciences, #560411) for 30 minutes on ice, protected
610 from light. Cells were then washed with FACS buffer (1:5), and resuspended in 300µl FACS buffer +
611 DAPI (Miltenyi Biotec, # 130-111-570) for live/dead cell identification. Cells were then analyzed using
612 a Sony MA900 Multi-application cell sorter. For analysis, cells were gated based on forward and side
613 scatter, followed by height and width parameters to identify singlets. Finally, DAPI-negative (live cells)
614 were gated for CD73 and CD144 populations.
615
616 **ATAC-seq**
617 HUVECs were cultured in medium 199 (Sigma-Aldrich, MO, USA) supplemented with 16% fetal
618 bovine serum (FBS), 100 U/ml penicillin, 100 U/ml streptomycin, 15 µg/ml endothelial cell growth
619 factor (BD Biosciences, MA, USA) and 15 µg/ml heparin (Sigma-Aldrich, MO, USA) at a humidified
620 37 ◦C, 5% CO2 incubator.

621 HUVECs were grown to 60% confluence then treated with 25uM Sm4 or the equivalent volume of
622 DMSO. 24 hours after treatment, 3 HUVEC lines were harvested and pooled. ATAC-seq and ATAC-
623 seq analysis were performed by Active Motif. As per their sample preparation instructions, 150k
624 cells/sample were collected, centrifuged at 500 x g at 4°C to remove the supernatant. Then, the cells
625 were resuspended in ice-cold cryopreservation solution (50% FBS, 40% media, and 10% DMSO) and
626 transferred to cryotubes for freezing. Samples were then shipped to Active Motif for analysis.

627 **HS17 sample preparation**
628 The human embryo samples were collected for pathological examination, which entails histological
629 verification of pregnancy and confirmation of fetal components. In addition, they were assessed to
630 ensure the absence of conditions such as hydatidiform mole or choriocarcinoma. We selected residual
631 specimens, collected between January 2000 and October 2021. The use of human samples was approved
632 by the Ethics Committee of Mie University Hospital (approval number: H2021-228). Informed consent
633 was acquired at the time of surgery, complemented by the availability of an opt-out provision, ensuring
634 participants' autonomy to withdraw from the study at any point. The staging of the embryos and fetuses
635 used in the experiments was done using a combination of the Tissue collection and ethical
636 considerations. For this study, 31 preserved human embryos in organogenesis period and 3 fetuses
637 ranging from CS8 to GW9 were analyzed. The samples were collected for pathological examination,
638 which entails histological verification of pregnancy (investigating the decidua's interstitial and the
639 endometrium's Arias-Stella reactions) and confirmation of fetal components (examination of chorionic
640 tissue). In addition, they were assessed to ensure the absence of conditions such as hydatidiform mole
641 or choriocarcinoma. We selected residual specimens, collected between January 2000 and October
642 2021, that included embryos and utilized these specimens specifically for the purposes of this research.
643
644 **Immunohistochemistry (IHC)**
645 ***Proband samples***
646 Prior to staining the samples were processed to remove paraffin wax through multiple xylene and
647 ethanol baths. Epitope retrieval was performed using Tris-EDTA. To stain the sample sections the
648 samples were submerged in blocking buffer consisting of 1M maleic acid (Sigma, M0375), 10% heat
649 inactivated horse serum (Sigma, H1138), 1% DMSO (Sigma, 472301), 0.1% PBTX (PBS + 0.1%
650 Tween-20) (Tween-20, Sigma, P7949) for 1hr. Antibodies were then diluted into blocking buffer at
651 1:50 for anti-hCD31 (Abcam, ab28364) and 1:250 for anti-hNR2F2 (R&D systems, PPH714700) and
652 anti-hSOX18 (Santa Cruz Biotechnology, sc-166025) overnight in the dark at 4C. The next day the
653 slides were washed in blocking buffer three times over the course of 30min. Secondary antibodies were
654 diluted in blocking buffer at 1:300 (ThermoFisher (Alexa Fluor 488 goat anti-rabbit IgG, A11008),
655 (Alexa Fluor 555 goat anti-mouse IgG2a, A21137), (Alexa Fluor 647 goat anti-mouse IgG1, A21240))

656 for 1hr at room temp in the dark. Samples were then washed with PBS three times over 30min. Hoechst
657 (ThermoFisher, R37605)) was diluted in PBS at 1:1000 and added to the slides for 10 min, then washed
658 twice with PBS and mounted. Imaging was performed on a Zeiss 800 LSM. All images were processed
659 using ImageJ software.
660
661 ***HS17 sample***
662 IHC was performed using 3-µm thick sections. The sections were deparaffinised and rehydrated through
663 a series of xylene and ethanol. To suppress autofluorescence, samples were incubated in 0.1% sodium
664 borohydride in 0.1M phosphate-buffered saline (PBS) (137 mM NaCl, 2.7 mM KCl, 10 mM Na2HPO4,
665 and 1.8 mM KH2PO4, pH 7.2) for 30 minutes, rinsed with water, and subsequently incubated for 5
666 minutes in 0.2M glycine in 0.1M PBS. Antigen retrieval was carried out using a pressure chamber with
667 Tris-EDTA buffer (7.4 mM Tris, 1 mM EDTA-2Na, pH 9.0). Slides were incubated with primary
668 antibodies against Prox1 (AF2727, R&D Systems, 1:150, RRID), Coup-TF2 (EPR18443, Abcam,
669 1:150, RRID), and SOX18 (sc-166025, Santa Cruz Biotechnology, 1:50, RRID). Alexa Fluor-
670 conjugated secondary antibodies (Abcam, 1:400) were subsequently applied. Imaging was carried out
671 using a Keyence BZ-X700 microscope. All images were processed using ImageJ software.

672 ***Immunofluorescent staining of IH, VM and AVM FFPE patient tissue sections***
673 FFPE tissue sections (5 µm) from patients with IH, VM or AVM were deparaffinized, immersed in an
674 antigen retrieval solution (citrate-EDTA buffer containing 10 mM citric acid, 2 mM EDTA, and
675 0.05% Tween-20, pH 6.2) for 20 minutes at 95°C–99°C, cooled down and washed. Blocked for 30
676 min was performed in 10% donkey serum followed by incubation overnight at 4C with monoclonal
677 IgG1 mouse anti-human SOX18 (D-8) (1:50, Santa Cruz Biotechnology, sc-166025), monoclonal
678 IgG_{2A} mouse anti-human COUP-TF II (1:100, R&D, PP-H7147-00), and UEA1 fluorescently labeled
679 with Alexa Fluor 649 (1:50, Vector Laboratories, DL1068). Next, the sections were incubated with
680 Alexa Fluor 546 goat anti-mouse IgG1 (1:200; cross-absorbed, Invitrogen, A-21123) and Alexa Fluor
681 488 goat anti-mouse IgG_{2A} (1:200; cross-absorbed, Invitrogen, A-21137) as secondary antibodies for
682 45 minutes at room temperature. All slides were mounted using DAPI (Molecular Probes) to visualize
683 nuclei. IF Images were acquired using a LSM 880 confocal microscope (Zeiss) through a 63x
684 objective lens. All images were analyzed using Fiji ImageJ software.
685
686 ***Immunofluorescent cell staining of HemSC, HemEC, and ECFC***
687 Hemangioma stem cells (HemSC), hemangioma endothelial cells (HemEC) and endothelial colony
688 forming cells (ECFC) were seeded on fibronectin-coated plates at a density of 30,000 cells/cm^2 in
689 EGM-2 media for 30 hours on 2 cm^2 slides, fixed in 4% PFA and blocked in 5% BSA/0.3% Triton x-
690 100 for 1 hour. Cells were co-stained for monoclonal IgG1 mouse anti-human SOX18 (D-8) (1:100,
691 Santa Cruz Biotechnology, sc-166025), monoclonal IgG_{2A} mouse anti-human COUP-TF II (1:200,
692 R&D, PP-H7147-00). Alexa Fluor 546 goat anti-mouse IgG1 (1:200; cross-absorbed, Invitrogen, A-
693 21123) and Alexa Fluor 488 goat anti-mouse IgG_{2A} (1:200; cross-absorbed, Invitrogen, A-21137)
694 served as secondary antibodies, incubation was for 45 minutes at room temperature. DAPI was used
695 to visualize nuclei (Molecular Probes) followed by mounting (Invitrogen). Immunostainings of IH
696 sections with respective isotype matched control IgG and secondary antibodies were conducted.
697
698 **RNA isolation and RT-qPCR**
699 ***hESC***
700 Total RNA was exracted using Trizol reagent (ThermoFisher Scientific, #1559608). RNA concentration
701 was determined using Nanodrop (Thermoscientific). cDNA was produced using verso cDNA synthesis
702 kit (ThermoFisher Scientific, 1453B). qPCR amplification was performed using PowerUP SYBR Green

703 (ThermoFischer Scientific, A25778) on a Quantstudio 7 Flex (ThermoFischer Scientific). The $2^{-\Delta\Delta CT}$
704 method was used to calculate relative gene expression relative to YWHAZ.
705
706 ***HUVEC drug treatment***
707 The day before collection 300k cells/well were seeded in a 6 well plate. The following day HUVECs
708 were treated with either CIA1 (Tocris, 7494) at 4µM or CIA1 at 4µM + R(+)propranolol (Sigma, P0689)
709 at 25µM for 4 hours prior to collection. After 4 hours cells were washed with PBS. RNA was extracted
710 using Trizol reagent (ThermoFisher, #1559618). RNA concentration was determined using Nanodrop
711 (Thermo Scientific). cDNA was produced using cDNA kit (Bio-Rad, 1725035) and qPCR amplification
712 was performed using SensiFAST SYBR kit (Bio-Rad, BIO-98050) on a Roche Lightcycler 480 II. The
713 $2^{-\Delta\Delta CT}$ method was used to calculate relative gene expression relative to GAPDH.
714
715 ***IH cells***
716 Total RNA was extracted from cells with the RNeasy Micro Extraction Kit (QIAGEN). Reverse
717 transcriptase reactions were performed using an iScript cDNA Synthesis Kit (Bio-Rad). qPCR was
718 performed using SYBR FAST ABI Prism 2× qPCR Master Mix (Kapa BioSystems). Amplification
719 was carried out in a QuantStudio 6 Flex Real-Time PCR System (Fisher Scientific). A relative
720 standard curve for each gene amplification was generated to determine the amplification efficiency,
721 with greater than 90% considered acceptable. Fold increases in gene expression were calculated
722 according to the ΔΔCt method, with each amplification reaction performed in duplicate or triplicate.
723 ATP5B was used as housekeeping gene expression reference. A list of all primer sequences used in
724 this study is attached below.

725
726 ***Primers***
727

Gene	Seq (5'-3')	Seq (3'-5')
APLNR	CTCTGGACCGTGTTTCGGAG	GGTACGTGTAGGTAGCCCACA
ATP5B	CCACTACCAAGAAGGGATCTATCA	GGGCAGGGTCAGTCAAGTC
CD144	AACGAGCAGGGCGAGTTCACCTTC	TAGGTGACCAGCTGCTCGTGGATC
CD31	CACCTGGCCCAGGAGTTTC	AGTACACAGCCTTGTTGCCATGT
DCBLD2	CTGAGAGTGGAACCCTTACA	CGAACTCTCTCTCCCATCTT
DIAPH3	GGACACTGACGGATGATATG	GTCTTCAGGTTGGGAAGTG
EPHB4	AGAGGCCGTACTGGGACATGAG	TCCAGCATGAGCTGGTGGAG
FAM171A1	ACGCTCTGCCACTCTAAT	GCCCTTCTCTGGAAATGAAC
GALNT1	CTAGCCACCTCCTTGATTTG	CAGGAAGTCCTCTCTCCTTT
GAPDH	CCCCGGTTTCTATAAATTGAGC	CACCTTCCCCATGGTGTCT
LMO7	AGGCCCTCCAAACATACT	GATTCTTCCTGCGGGTTATG
MBNL1	GGTACTAAGAAGTGCCTTTCC	TGCTGTCGTCACAGTCTA
NR2F2	CCATAGTCCTGTTCACCTCAGA	AATCTCGTCGGCTGGTTG
NRP2	GCTGGCTATATCACCTCTCCC	TCTCGATTTCAAAGTGAGGGTTG
NT5E	CCAGTACCAGGGCACTATCTG	TGGCTCGATCAGTCCTTCCA
SLC26A4	GACGTCATTTCGGGAGTTAG	AGCAGAGTAGAGACCATATCC
SLC45A1	CCATCCTCGGATTCCTACT	CCCTATAGCCAGGACAAGA
SOX17	CAGAATCCAGACCTGCACAA	GCGGCCGGTACTTGTAGTT
SOX18	AAGCGTGGAAGGAGCTGAAC	CGCGGCCGGTACTTGTAGTT
SOX7	TCGACGCCCTGGATCAACT	CTGGGAGACCGGAACATGC

THBS1	CAACTCTCACAGCGACATT	CCTCCCTCATCCACATTTAC
YWHAZ	ACCGTTACTTGGCTGAGGTTGC	CCCAGTCTGATAGGATGTGTTGG

728
729 **NR2F2^{c994del} Plasmid creation**
730 Halo-NR2F2^{WT} (Genecopoeia, EX-C0221-M49) was used as a template to construct the c994del variant
731 plasmid using the megaprimer sight-directed mutagenesis method. The Halo-NR2F2^{c994del} plasmid was
732 validated by sanger sequencing to ensure the deletion occurred at position at 994.
733
734 **Quantitative molecular imaging**
735
736 **Single-molecule tracking (SMT)**
737 ***SMT Sample preparation***
738 Single-molecule tracking was performed as described in McCann et al.[48]. HeLa cells were seeded at a
739 density of 23,000 cells/well in 8-well chamber glass slides (Ibidi, 80827) coated with 0.5% gelatine 24h
740 prior to transfection. 300ng of plasmid DNA/well of either Halo-tagged NR2F2^{WT} or NR2F2^{c994del} was
741 transiently transfected into the cells using X-tremeGENE 9 Transfection Reagent kit (Roche,
742 XTG9RO). For dual transfection experiments 600ng (300ng of each plasmid) of plasmid DNA/well of
743 Halo-tagged NR2F2^{WT} + eGFP-SOX18, NR2F2^{c994del} + eGFP-SOX18, Halo-tagged SOX18 + eGFP-
744 NR2F2^{WT}, or SOX18 + eGFP-NR2F2^{c994del}. Cells were then incubated at 37°C with 5% CO_2 overnight
745 prior to imaging then washed three times and then incubated in imaging media (Fluorobrite DMEM
746 (Glibco), 10% FBS, 1% HEPES, 1% GlutaMax) 45 min prior to imaging 1nM of JF549 Halo-tag ligand
747 (Promega, GA1111) was added directly to the media and cells were incubated for 10 minutes at 37 ° C
748 with 5% of CO_2. Following incubation, cells were washed twice 15min apart and replaced with imaging
749 media.
750
751 ***SMT acquisition***
752 Images were acquired on a Nikon TIRF microscope at a TIRF angle of 61 degrees to achieve HILO
753 illumination. Samples were recorded with an iXon Ultra 888 EMCCD camera, filter cube TRF49909 –
754 ET – 561 laser bandpass filter and 100 X oil 1.49 NA TIRF objective. Cells were imaged using a 561nm
755 excitation laser at a power density of 10.3 µW to perform two different acquisition techniques. A fast
756 frame rate which uses a 50 Hz (20ms acquisition speed) to acquire 6000 frames without intervals to
757 measure displacement distribution and fraction bound, and a slow frame rate which uses a 2 Hz (500ms
758 acquisition speed) to acquire 500 frames without intervals to measure residence times.
759
760 ***SMT analysis***
761 Masking and segmentation of the nucleus was performed in ImageJ for all files. To identify and track
762 molecules a custom-written MATLAB implementation of the multiple target tracing (MTT) algorithm,
763 known as SLIMfast was used[81]. Parameters used for fast frame rate analysis: Localization error: $10^{-6.5}$,
764 blinking (frames) = 1, max # of competitors: 3, max expected diffusion coefficient = 3µm^2/sec, box size
765 = 7, timepoints = 7, clip factor = 4. Cells with less than 500 trajectories based on the above parameters
766 were excluded from analysis. The first four frames of each trajectory were used to calculate the mean
767 squared displacement. Diffusion coefficient was calculated from each trajectory's mean squared
768 displacement and plotted. An inflection point was determined on WT NR2F2 diffusion profile and used
769 as a boundary to determine confined vs non-confined states for all conditions. The confined fraction
770 and non-confined fraction of each cell were calculated by computing the number of trajectories whose
771 mean diffusion coefficient were defined as confined and non-confined respectively. Parameters used
772 for slow frame rate analysis: Localization error: 10^{-7}, blinking (frames): 1, max # of competitors: 3, max
773 expected diffusion coefficient = 0.33µm^2/sec, box size = 9. Slow-tracking analysis was performed using
774 custom MATLAB code based on [52].

775
776
777

Fluorescence fluctuation spectroscopy (FFS)

Halo Tag labelling for FFS experiment

To saturate all Halo Tags with Janelia Farm dyes 549 or 646 for single or dual-color labelling, HeLa cells transiently expressing Halo Tag-tagged Sox7, NR2F2 or NR2F2_C994del constructs were incubated with a saturating concentration of a single JF dye (JF549, 100 nM) or two JF dyes (JF549 : JF646, 100 nM : 100 nM) for 15 minutes at 37 °C, similar to McCann et al.[48]. Cells were washed twice with 1× PBS before imaging experiments.

FFS acquisition

All FFS measurements for Number and Brightness (NB) analysis and cross Raster Image Correlation Spectroscopy (RICS) were performed on an Olympus FV3000 laser scanning microscope coupled to an ISS A320 Fast FLIM box for fluorescence fluctuation data acquisition. For single channel NB FFS measurements, HaloJF549 tagged plasmids were excited by a solid-state laser diode operating at 561 nm and the resulting fluorescence signal was directed through a 405/488/561 dichroic mirror to an external photomultiplier detector (H7422P-40 of Hamamatsu) fitted with a mCherry 600-640 nm bandwidth filter. For dual channel RICS FFS measurements (that enable cross RICS), the HaloJF546 and HaloJF646 combination were excited by solid-state laser diodes operating at 561 nm and 640 nm, respectively, and the resulting signal was directed through a 405/488/561/640 dichroic mirror to two internal GaAsP photomultiplier detectors set to collect 600-640 nm and 650-750 nm, respectively.
All FFS data acquisitions (i.e., NB, cross RICS) employed a 60X water immersion objective (1.2 NA) and first involved selecting a 10.6 µm region of interest (ROI) within a HeLa cell nucleus at 37 °C in 5% CO2 that exhibited low protein expression level (nanomolar) to ensure observation of fluctuations in fluorescence intensity[82]. Then a single or simultaneous two channel frame scan acquisition was acquired (N = 100 frames) in the selected ROI with a pixel frame size of 256 x 256 (i.e., pixel size ~ 41nm) and a pixel dwell time of 12.5 µs. These conditions resulted in scanning pattern that was found to be optimal for simultaneous capture of the apparent brightness and mobility of the Halo tagged constructs being characterised by NB and cross RICS analysis; all of which was performed in the SimFCS software developed at the Laboratory for Fluorescence Dynamics (LFD).

Number and brightness (NB) analysis

The oligomeric state of the different HaloJF549-tagged plasmids investigated was extracted and spatially mapped throughout single channel FFS measurements via a moment-based brightness analysis that has been described in previously published papers [83,84]. In brief, within each pixel of an NB FFS measurement there is an intensity fluctuation $F(t)$ which has: (1) an average intensity $\langle F(t) \rangle$ (first moment) and (2) variance σ^2 (second moment); and the ratio of these two properties describes the apparent brightness (B) of the molecules that give rise to the intensity fluctuation. The true molecular brightness (ε) of the fluorescent molecules being measured is related to B by $B = \varepsilon + 1$, where 1 is the brightness contribution of a photon counting detector. Thus, if we measure the B of monomeric HaloJF549-Sox7 ($B_{monomer} = \varepsilon_{monomer} + 1$) under our NB FFS measurement conditions, then we can determine $\varepsilon_{monomer}$ and extrapolate the expected B of HaloJF549-tagged dimers ($B_{dimer} = (2 \times \varepsilon_{monomer}) + 1$) or oligomers (e.g., $B_{tetramer} = (4 \times \varepsilon_{monomer}) + 1$), *and in turn define* brightness cursors, to extract and spatially map the fraction of pixels within a NB FFS measurement that contain these different species. These cursors were used to extract the fraction of HaloJF549-NR2F2 dimer and oligomer (i.e., number of pixels assigned B_{dimer} or $B_{oligomer}$) within a NB FFS measurement and quantify the degree of NR2F2 self-association across multiple cells. Artefact due to cell movement or photobleaching were subtracted from acquired intensity fluctuations via use of a moving average algorithm and all brightness analysis was carried out in SimFCS from the Laboratory for Fluorescence Dynamics.

Cross RICS analysis

The fraction of interaction between the HaloJF549 and HaloJF646-tagged NR2F2 or NR2F2-C994del plasmids was extracted via application of cross RICS functions described in previously published papers to the dual channel FFS measurements[48,82]. In brief, the fluorescence intensity recorded within each frame (N =100) of each channel (i.e., CH1 and CH2) was spatially correlated via application of the RICS function, and spatially cross-correlated between channels (CC) via application of the cross RICS function, alongside a moving average algorithm (N = 10 frames) in both instances. Then the

recovered RICS and cross RICS correlation profiles were fit to a 3D diffusion model and the amplitude versus decay of each fit recorded in the form of a G value and diffusion coefficient (D) respectively. The ratio of the cross RICS amplitude (i.e., G_{CC}) with the limiting channel RICS amplitude (i.e., G_{CH1} or G_{CH2}) enabled the fraction of HaloJF549-NR2F2 molecules interacting with Halo646-NR2F2 molecules to be extracted. All cross RICS analysis was carried out in SimFCS from the Laboratory for Fluorescence Dynamics.

Statistics

All statistical analyses were performed using GraphPad Prism. An outlier test using settings (Q=1) was performed to identify and remove outliers. Results are displayed as mean ± the standard deviation unless indicated otherwise.

Study approvals and ethics

Proband samples The use of the proband's samples was approved by the Hunter New England Exemption from HREC case study (authorization number: AU2206-11). All procedures were conducted in compliance with guidelines and regulations. ***hESCs*** The use of human embryonic stem cells (hESCs) in this study was approved by Stem Cell Research Oversight (SCRO) at Stanford University. All procedures were conducted in compliance with institutional guidelines and regulations. ***CS17 sample*** The use of human samples was approved by the Ethics Committee of Mie University Hospital (approval number: H2021-228). Informed consent was acquired at the time of surgery, complemented by the availability of an opt-out provision, ensuring participants' autonomy to withdraw from the study at any point. ***HemSC, HemEC, and ECFC*** Vascular anomaly specimens were obtained under protocols approved by the Committee on Clinical Investigation at Boston Children's Hospital (IRB protocol number 04-12-175R and P00003505; AH, JB). Patient specimens were collected upon written informed consent of the patient or the patient's guardian, de-identified, and used for cell isolation as well as tissue staining under a Boston Children's Hospital IRB approved protocol (04-12-175R and P00003505) and in accordance with Declaration of Helsinki principles. ***HUVEC cells*** Umbilical cords were collected from the Royal Prince Alfred Hospital upon written informed consent of the patient or the patient's guardian, de-identified, and used for cell isolation of human umbilical vein endothelial cells (HUVECs). Isolation protocol was as previously described in Litwin et al.[85] and cells were used from passage 1 to 3. Ethics approval for the collection of the umbilical cords was from SLHD Protocol No. X16-0225.

Data Availability

The data that supports the findings in this study are available at DOI: 10.5281/zenodo.15098820.

880 References:

881 1. You, L.-R. *et al.* Suppression of Notch signalling by the COUP-TFII transcription factor regulates
882 vein identity. *Nature* **435**, 98–104 (2005).
883 2. McCracken, I. R., Baker, A. H., Smart, N. & De Val, S. Transcriptional regulators of arterial and
884 venous identity in the developing mammalian embryo. *Current Opinion in Physiology* **35**, 100691
885 (2023).
886 3. Swift, M. R. *et al.* SoxF factors and Notch regulate *nr2f2* gene expression during venous
887 differentiation in zebrafish. *Developmental Biology* **390**, 116–125 (2014).
888 4. Aranguren, X. L. *et al.* COUP-TFII orchestrates venous and lymphatic endothelial identity by
889 homo- or hetero-dimerisation with PROX1. *Journal of Cell Science* **126**, 1164–1175 (2013).
890 5. Aranguren, X. L. *et al.* Transcription factor COUP-TFII is indispensable for venous and
891 lymphatic development in zebrafish and *Xenopus laevis*. *Biochemical and Biophysical Research*
892 *Communications* **410**, 121–126 (2011).
893 6. Lin, F.-J. *et al.* Endocardial Cushion Morphogenesis and Coronary Vessel Development Require
894 Chicken Ovalbumin Upstream Promoter-Transcription Factor II. *Arterioscler Thromb Vasc Biol*
895 **32**, e135–e146 (2012).
896 7. Pereira, F. A., Qiu, Y., Zhou, G., Tsai, M.-J. & Tsai, S. Y. The orphan nuclear receptor COUP-
897 TFII is required for angiogenesis and heart development. *Genes Dev* **13**, 1037–1049 (1999).
898 8. Su, T. *et al.* Single-cell analysis of early progenitor cells that build coronary arteries. *Nature* **559**,
899 356–362 (2018).
900 9. Wang, J. *et al.* NR2F2 loss-of-function mutation is responsible for congenital bicuspid aortic
901 valve. *International Journal of Molecular Medicine* **43**, 1839–1846 (2019).
902 10. Qiao, X.-H. *et al.* A novel NR2F2 loss-of-function mutation predisposes to congenital heart
903 defect. *European Journal of Medical Genetics* **61**, 197–203 (2018).
904 11. Al Turki, S. *et al.* Rare Variants in NR2F2 Cause Congenital Heart Defects in Humans. *Am J*
905 *Hum Genet* **94**, 574–585 (2014).
906 12. High, F. A. *et al.* De novo frameshift mutation in COUP-TFII (NR2F2) in human congenital
907 diaphragmatic hernia. *American Journal of Medical Genetics Part A* **170**, 2457–2461 (2016).

908 13. Bashamboo, A. *et al.* Loss of Function of the Nuclear Receptor NR2F2, Encoding COUP-TF2,
909 Causes Testis Development and Cardiac Defects in 46,XX Children. *The American Journal of*
910 *Human Genetics* **102**, 487–493 (2018).
911 14. Chen, X., Qin, J., Cheng, C.-M., Tsai, M.-J. & Tsai, S. Y. COUP-TFII Is a Major Regulator of
912 Cell Cycle and Notch Signaling Pathways. *Molecular Endocrinology* **26**, 1268–1277 (2012).
913 15. Sissaoui, S. *et al.* Genomic Characterization of Endothelial Enhancers Reveals a Multifunctional
914 Role for NR2F2 in Regulation of Arteriovenous Gene Expression. *Circulation Research* **126**,
915 875–888 (2020).
916 16. Kumarasamy, S. *et al.* Mutation within the hinge region of the transcription factor Nr2f2
917 attenuates salt-sensitive hypertension. *Nat Commun* **6**, 6252 (2015).
918 17. Dinh, T. T. *et al.* An NKX-COUP-TFII morphogenetic code directs mucosal endothelial
919 addressin expression. *Nat Commun* **13**, 7448 (2022).
920 18. Overman, J. *et al.* Pharmacological targeting of the transcription factor SOX18 delays breast
921 cancer in mice. *eLife* **6**, e21221.
922 19. Srinivasan, R. S. *et al.* The nuclear hormone receptor Coup-TFII is required for the initiation and
923 early maintenance of Prox1 expression in lymphatic endothelial cells. *Genes Dev.* **24**, 696–707
924 (2010).
925 20. Duong, T. *et al.* VEGFD regulates blood vascular development by modulating SOX18 activity.
926 *Blood* **123**, 1102–1112 (2014).
927 21. Fontijn, R. D. *et al.* SOX-18 controls endothelial-specific claudin-5 gene expression and barrier
928 function. *American Journal of Physiology-Heart and Circulatory Physiology* **294**, H891–H900
929 (2008).
930 22. Garcia-Flores, A. E. *et al.* Loss of SOX18/CLAUDIN5 disrupts the pulmonary endothelial barrier
931 in ventilator-induced lung injury. *Front Physiol* **13**, 1066515 (2022).
932 23. François, M. *et al.* Sox18 induces development of the lymphatic vasculature in mice. *Nature* **456**,
933 643–647 (2008).
934 24. Patel, J. *et al.* Functional Definition of Progenitors Versus Mature Endothelial Cells Reveals Key
935 SoxF-Dependent Differentiation Process. *Circulation* **135**, 786–805 (2017).

936 25. Donovan, P. *et al.* Endovascular progenitors infiltrate melanomas and differentiate towards a
937 variety of vascular beds promoting tumor metastasis. *Nat Commun* **10**, 18 (2019).
938 26. Duong, T. *et al.* Genetic Ablation of SOX18 Function Suppresses Tumor Lymphangiogenesis and
939 Metastasis of Melanoma in Mice. *Cancer Research* **72**, 3105–3114 (2012).
940 27. Moalem, S. *et al.* Hypotrichosis-lymphedema-telangiectasia-renal defect associated with a
941 truncating mutation in the SOX18 gene. *Clin Genet* **87**, 378–382 (2015).
942 28. Dailey, C., Oshodi, R. B., Boull, C. & Aggarwal, A. Expanding the clinical spectrum of *SOX18*-
943 related Hypotrichosis-lymphedema-telangiectasia-renal defect syndrome. *European Journal of*
944 *Medical Genetics* **65**, 104607 (2022).
945 29. Chen, J. *et al.* SOX18 promotes gastric cancer metastasis through transactivating MCAM and
946 CCL7. *Oncogene* **39**, 5536–5552 (2020).
947 30. Seebauer, C. T. *et al.* Non–beta blocker enantiomers of propranolol and atenolol inhibit
948 vasculogenesis in infantile hemangioma. *J Clin Invest* **132**, (2022).
949 31. Overman, J. *et al.* R-propranolol is a small molecule inhibitor of the SOX18 transcription factor
950 in a rare vascular syndrome and hemangioma. *Elife* **8**, e43026 (2019).
951 32. Fontaine, F. *et al.* Small-Molecule Inhibitors of the SOX18 Transcription Factor. *Cell Chemical*
952 *Biology* **24**, 346–359 (2017).
953 33. Holm, A. *et al.* An endothelial SOX18-mevalonate pathway axis enables repurposing of statins
954 for infantile hemangioma. *J Clin Invest* (2025) doi:10.1172/JCI179782.
955 34. Fu, X. & Rabadan, R. Understanding variants of unknown significance: the computational
956 frontier. *The Oncologist* **29**, 653–657 (2024).
957 35. Zaidi, S. & Brueckner, M. Genetics and Genomics of Congenital Heart Disease. *Circ Res* **120**,
958 923–940 (2017).
959 36. Eifert, S., Villavicencio, J. L., Kao, T.-C., Taute, B. M. & Rich, N. M. Prevalence of deep venous
960 anomalies in congenital vascular malformations of venous predominance. *Journal of Vascular*
961 *Surgery* **31**, 462–471 (2000).

962 37. Tasnádi, G. Epidemiology of Vascular Malformations. in *Hemangiomas and Vascular*
963 *Malformations: An Atlas of Diagnosis and Treatment* (eds. Mattassi, R., Loose, D. A. & Vaghi,
964 M.) 109–110 (Springer Milan, Milano, 2009). doi:10.1007/978-88-470-0569-3_14.
965 38. Zhang, P. *et al.* Negative cross-talk between hematopoietic regulators: GATA proteins repress
966 PU.1. *Proc Natl Acad Sci U S A* **96**, 8705–8710 (1999).
967 39. Rekhtman, N., Radparvar, F., Evans, T. & Skoultchi, A. I. Direct interaction of hematopoietic
968 transcription factors PU.1 and GATA-1: functional antagonism in erythroid cells. *Genes Dev* **13**,
969 1398–1411 (1999).
970 40. Peck, B., Ferber, E. C. & Schulze, A. Antagonism between FOXO and MYC Regulates Cellular
971 Powerhouse. *Front Oncol* **3**, 96 (2013).
972 41. Mukherjee, S., Luedeke, D. M., McCoy, L., Iwafuchi, M. & Zorn, A. M. SOX transcription
973 factors direct TCF-independent WNT/β-catenin responsive transcription to govern cell fate in
974 human pluripotent stem cells. *Cell Reports* **40**, 111247 (2022).
975 42. Ang, L. T. *et al.* Generating human artery and vein cells from pluripotent stem cells highlights the
976 arterial tropism of Nipah and Hendra viruses. *Cell* **185**, 2523-2541.e30 (2022).
977 43. Deng, Y., Atri, D., Eichmann, A. & Simons, M. Endothelial ERK signaling controls lymphatic
978 fate specification. *J Clin Invest* **123**, 1202–1215 (2013).
979 44. Ibarra-Soria, X. *et al.* Defining murine organogenesis at single-cell resolution reveals a role for
980 the leukotriene pathway in regulating blood progenitor formation. *Nat Cell Biol* **20**, 127–134
981 (2018).
982 45. Moustaqil, M. *et al.* Homodimerization regulates an endothelial specific signature of the SOX18
983 transcription factor. *Nucleic Acids Res* **46**, 11381–11395 (2018).
984 46. Jumper, J. *et al.* Highly accurate protein structure prediction with AlphaFold. *Nature* **596**, 583–
985 589 (2021).
986 47. Cheng, J. *et al.* Accurate proteome-wide missense variant effect prediction with AlphaMissense.
987 *Science* (2023) doi:10.1126/science.adg7492.
988 48. McCann, A. J. *et al.* A dominant-negative SOX18 mutant disrupts multiple regulatory layers
989 essential to transcription factor activity. *Nucleic Acids Res* **49**, 10931–10955 (2021).

990 49. Digman, M. A. & Gratton, E. Lessons in Fluctuation Correlation Spectroscopy. *Annu Rev Phys*
991 *Chem* **62**, 645–668 (2011).
992 50. Digman, M. A., Dalal, R., Horwitz, A. F. & Gratton, E. Mapping the Number of Molecules and
993 Brightness in the Laser Scanning Microscope. *Biophys J* **94**, 2320–2332 (2008).
994 51. Hinde, E. *et al.* Quantifying the dynamics of the oligomeric transcription factor STAT3 by pair
995 correlation of molecular brightness. *Nat Commun* **7**, 11047 (2016).
996 52. Chen, J. *et al.* Single-Molecule Dynamics of Enhanceosome Assembly in Embryonic Stem Cells.
997 *Cell* **156**, 1274–1285 (2014).
998 53. Dunham, I. *et al.* An integrated encyclopedia of DNA elements in the human genome. *Nature*
999 **489**, 57–74 (2012).
1000 54. McLean, C. Y. *et al.* GREAT improves functional interpretation of cis-regulatory regions. *Nat*
1001 *Biotechnol* **28**, 495–501 (2010).
1002 55. Tanigawa, Y., Dyer, E. S. & Bejerano, G. WhichTF is functionally important in your open
1003 chromatin data? *PLOS Computational Biology* **18**, e1010378 (2022).
1004 56. Wang, L. *et al.* Small-molecule inhibitor targeting orphan nuclear receptor COUP-TFII for
1005 prostate cancer treatment. *Science Advances* **6**, eaaz8031 (2020).
1006 57. Kruse, S. W. *et al.* Identification of COUP-TFII Orphan Nuclear Receptor as a Retinoic Acid–
1007 Activated Receptor. *PLOS Biology* **6**, e227 (2008).
1008 58. Bryant, P., Pozzati, G. & Elofsson, A. Improved prediction of protein-protein interactions using
1009 AlphaFold2. *Nat Commun* **13**, 1265 (2022).
1010 59. Mirdita, M. *et al.* ColabFold: making protein folding accessible to all. *Nat Methods* **19**, 679–682
1011 (2022).
1012 60. Calvo, K. R. & Hickstein, D. D. The spectrum of GATA2 deficiency syndrome. *Blood* **141**,
1013 1524–1532 (2023).
1014 61. Mellor, R. H. *et al.* Mutations in FOXC2 Are Strongly Associated With Primary Valve Failure in
1015 Veins of the Lower Limb. *Circulation* **115**, 1912–1920 (2007).

1016 62. Irrthum, A. *et al.* Mutations in the Transcription Factor Gene SOX18 Underlie Recessive and
1017 Dominant Forms of Hypotrichosis-Lymphedema-Telangiectasia. *Am J Hum Genet* **72**, 1470–
1018 1478 (2003).
1019 63. Valenzuela, I. *et al.* Further delineation of the *SOX18*-related Hypotrichosis, Lymphedema,
1020 Telangiectasia syndrome (HTLS). *European Journal of Medical Genetics* **61**, 269–272 (2018).
1021 64. Schrenk, S. & Boscolo, E. A transcription factor is the target of propranolol treatment in infantile
1022 hemangioma. https://www.jci.org/articles/view/156863/pdf (2022) doi:10.1172/JCI156863.
1023 65. Tuohinto, K. *et al.* Oncogenic virus hijacks SOX18 pioneer function to enhance viral persistence.
1024 2025.06.28.662102 Preprint at https://doi.org/10.1101/2025.06.28.662102 (2025).
1025 66. Gramolelli, S. *et al.* Oncogenic Herpesvirus Engages Endothelial Transcription Factors SOX18
1026 and PROX1 to Increase Viral Genome Copies and Virus Production. *Cancer Res* **80**, 3116–3129
1027 (2020).
1028 67. Tuohinto, K. *et al.* KSHV infection of endothelial precursor cells with lymphatic characteristics
1029 as a novel model for translational Kaposi's sarcoma studies. *PLoS Pathog* **19**, e1010753 (2023).
1030 68. Henley, M. J. & Koehler, A. N. Advances in targeting 'undruggable' transcription factors with
1031 small molecules. *Nat Rev Drug Discov* **20**, 669–688 (2021).
1032 69. McSwiggen, D. T. *et al.* A high-throughput platform for single-molecule tracking identifies drug
1033 interaction and cellular mechanisms. *eLife* **12**, RP93183 (2025).
1034 70. Watanabe, D., Hiroshima, M., Yasui, M. & Ueda, M. Single molecule tracking based drug
1035 screening. *Nat Commun* **15**, 8975 (2024).
1036 71. Marziano, C., Genet, G. & Hirschi, K. K. Vascular endothelial cell specification in health and
1037 disease. *Angiogenesis* **24**, 213–236 (2021).
1038 72. Krebs, L. T. *et al.* Haploinsufficient lethality and formation of arteriovenous malformations in
1039 Notch pathway mutants. *Genes Dev* **18**, 2469–2473 (2004).
1040 73. Lin, Y. *et al.* Role of endothelial PDGFB in arterio-venous malformations pathogenesis.
1041 *Angiogenesis* **27**, 193–209 (2024).
1042 74. Chiang, I. K.-N. *et al.* SoxF factors induce Notch1 expression via direct transcriptional regulation
1043 during early arterial development. *Development* **144**, 2629–2639 (2017).

1044 75. Sacilotto, N. *et al.* Analysis of Dll4 regulation reveals a combinatorial role for Sox and Notch in
1045 arterial development. *Proc Natl Acad Sci U S A* **110**, 11893–11898 (2013).
1046 76. Coelho-Santos, V. & Shih, A. Y. Postnatal development of cerebrovascular structure and the
1047 neurogliovascular unit. *WIREs Developmental Biology* **9**, e363 (2020).
1048 77. Hammill, A. M. *et al.* Sirolimus for the treatment of complicated vascular anomalies in children.
1049 *Pediatric Blood & Cancer* **57**, 1018–1024 (2011).
1050 78. Seront, E. *et al.* Preliminary results of the European multicentric phase III trial regarding
1051 sirolimus in slow-flow vascular malformations. *JCI Insight* **8**, e173095.
1052 79. Geeurickx, M. & Labarque, V. A narrative review of the role of sirolimus in the treatment of
1053 congenital vascular malformations. *Journal of Vascular Surgery: Venous and Lymphatic*
1054 *Disorders* **9**, 1321–1333 (2021).
1055 80. Loh, K. M. *et al.* Protocol for efficient generation of human artery and vein endothelial cells from
1056 pluripotent stem cells. *STAR Protocols* **6**, 103494 (2025).
1057 81. Sergé, A., Bertaux, N., Rigneault, H. & Marguet, D. Dynamic multiple-target tracing to probe
1058 spatiotemporal cartography of cell membranes. *Nat Methods* **5**, 687–694 (2008).
1059 82. Lou, J. *et al.* Heterochromatin protein 1 alpha (HP1α) undergoes a monomer to dimer transition
1060 that opens and compacts live cell genome architecture. *Nucleic Acids Res* **52**, 10918–10933
1061 (2024).
1062 83. Hinde, E., Cardarelli, F. & Gratton, E. Spatiotemporal regulation of Heterochromatin Protein 1-
1063 alpha oligomerization and dynamics in live cells. *Sci Rep* **5**, 12001 (2015).
1064 84. Lou, J., Priest, D. G., Solano, A., Kerjouan, A. & Hinde, E. Spatiotemporal dynamics of 53BP1
1065 dimer recruitment to a DNA double strand break. *Nat Commun* **11**, 5776 (2020).
1066 85. Litwin, M. *et al.* Novel Cytokine-independent Induction of Endothelial Adhesion Molecules
1067 Regulated by Platelet/Endothelial Cell Adhesion Molecule (CD31). *J Cell Biol* **139**, 219–228
1068 (1997).
1069
1070
1071
1072

Acknowledgments
We thank the Vascular Anomalies Center and Department of Pathology at Boston's Children's Hospital for patient specimens. We acknowledge the technical and scientific staff of Sydney Microscopy & Microanalysis, the University of Sydney node of Microscopy Australia. Research reported in this manuscript was supported by NIH-R01HL12850307 (SJ), University of Sydney Drug Discovery Initiative - seed funding (grant ID: 23059) (MG, PC), Australian Excellence in Diversity Fellowship (JQ), the Vascular Anomalies Center at Boston Children's Hospital (AH), and the Grants-in-Aid for Scientific Research from the Ministry of Education, Culture, Sports, Science, and Technology of Japan (23K15949) and Japan Agency for Medical Research and Development (AMED) (22jm0610079h0001) (KM). KRH was supported by NIH-R01HL12850307 and the Howard Hughes Medical Institute. NHMRC Idea Grants (APP2019904 and APP2029719) (MF)

Author contributions
MG, SJ, MF, and KRH designed the study. MF coordinated the studies with all laboratories and provided the original idea of pharmacological rescue. GM coordinated the interaction between SK and MF. MG, SJ, JQ, AH, PC, TK, WL, and KM conducted experiments. MG, SJ, JQ, AH, YW, and KM carried out formal analysis. AH, SN, ES, TD, and KM provided samples, clinical management, and ethics. MG, AH, EH, and KM performed data curation. MG and MF wrote the original manuscript. All authors reviewed, edited, and agreed to the final version of the manuscript. MF and KRH acquired funding.

Conflict-of-interest statement
MF is on the scientific advisory board of Gertrude Biomedical Pty Ltd., and a shareholder of the company. TK is the CEO of Gertrude Biomedical Pty Ltd. All other authors declare no competing interests.

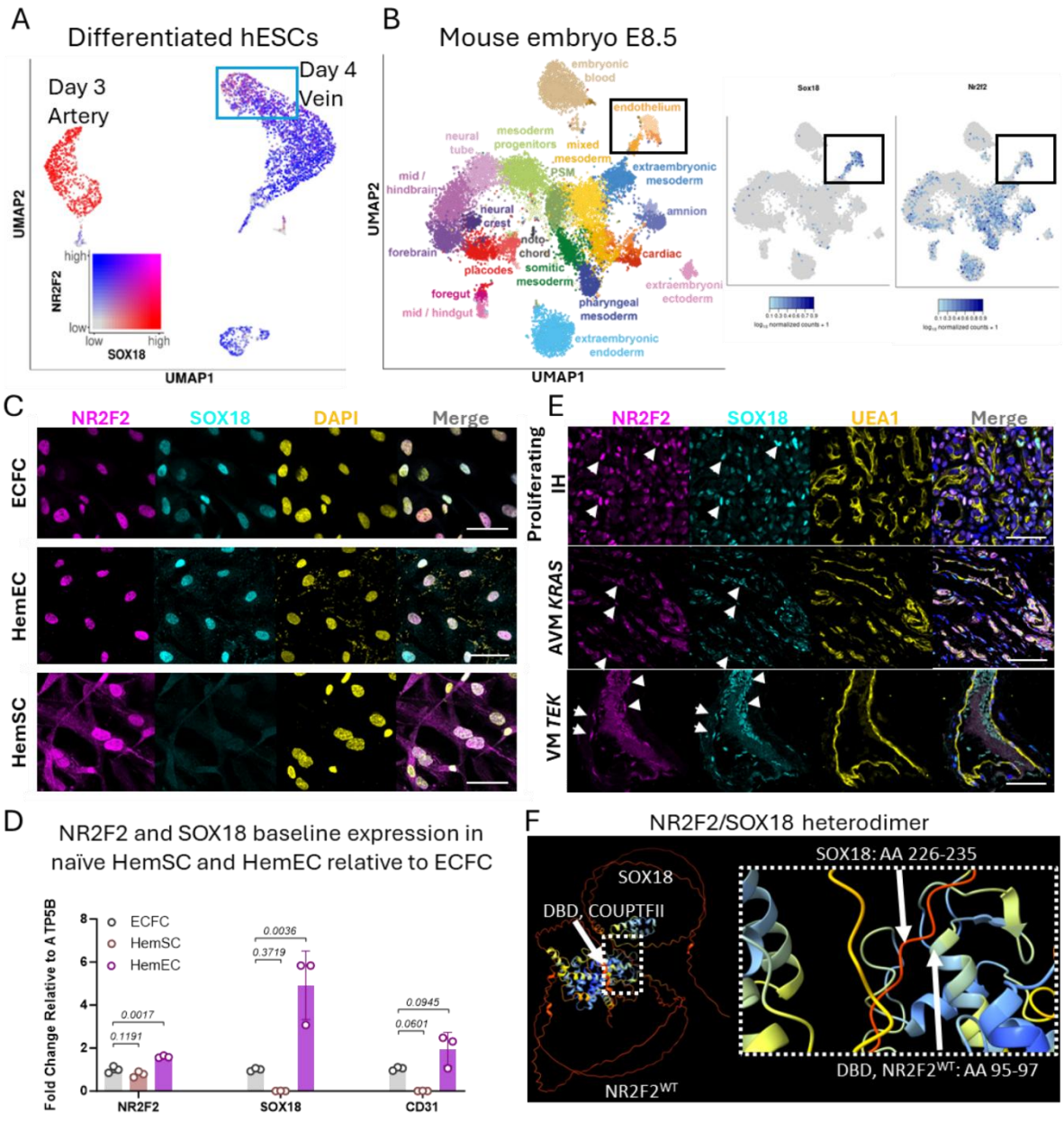

Supp Fig 1: *In vivo* SOX18 and NR2F2 are co expressed during human development and vascular malformations. A UMAP of NR2F2 and SOX18 from scRNA-seq dataset from Ang et al. of ECs derived from hESCs. Blue box denotes venous population expressing both NR2F2 and SOX18. **B** UMAP of NR2F2 and SOX18 from scRNA-seq dataset from Ibarra-Soria et al. of mouse embryo at E8.5. **C** Immunofluorescent staining of NR2F2 (magenta) and SOX18 (cyan), and nuclei stained with DAPI (yellow) in IH patient-derived hemangioma stem cells (HemSC), hemangioma endothelial cells (HemEC), and ECFC demonstrates nuclear co-expression (scale bars 25 µm). **D** qPCR comparing mRNA levels of NR2F2 and SOX18 in patient-derived HemSC and HemEC relative to ECFC (n=3 biological replicates for HemSC and HemEC, n=3 independent experiments for ECFC; P values were calculated using one-way ANOVA with Dunnett's multiple comparisons test. Data show the mean ± SD. **E** Immunofluorescent staining of NR2F2 (magenta), SOX18 (cyan), and the endothelial marker UEA1 (yellow) in IH, VM, and AVM patient tissue. White arrows denote nuclear co-expression of NR2F2 and SOX18 in EC (scale bars 50 µm). **F** Alphafold 2 modeling of $NR2F2^{WT}$ and SOX18 (left). Dimer formation occurs at amino acids 95-97 (DNA binding domain) on $NR2F2^{WT}$ and at amino acid 226-235 (TAD) on SOX18.

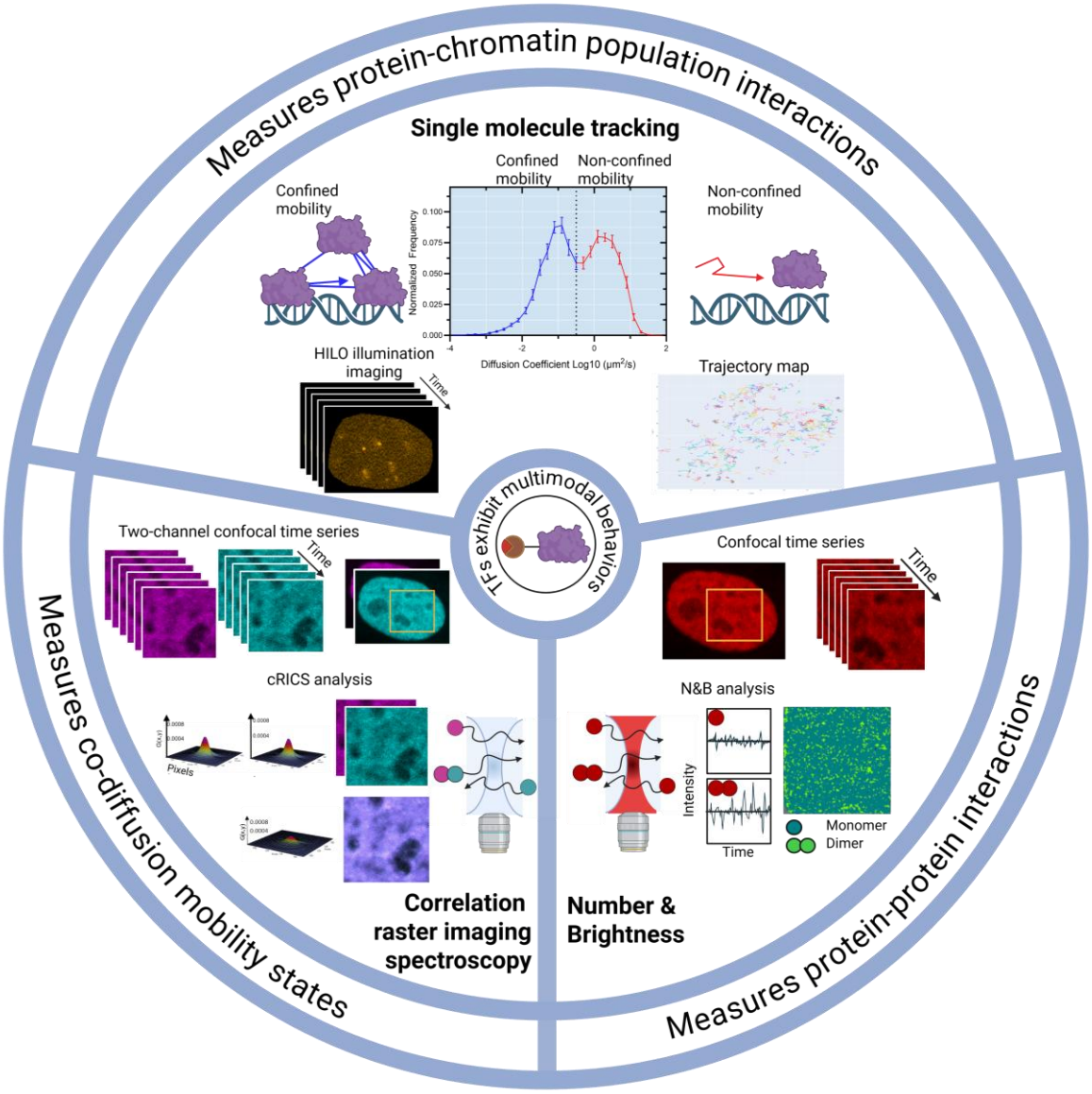

Supp Fig 2: Biophysical features of transcription factors behavior involved in gene regulation. TFs exhibit distinct multimodal behaviors that reflect their functional roles, including chromatin interactions and PPI. To investigate these behaviors we applied the same imaging approaches described in McCann et al. Aligning the various dynamic behaviors provides a more comprehensive understanding of how the TFs navigate and interact within the nuclear environment.

Single molecule tracking (SMT). SMT was performed by acquiring time-lapse images of sparsely labeled fluorescent molecules using HILO illumination. In each frame, the position of individual fluorescent molecules was identified, and trajectories were reconstructed by linking positions across consecutive frames. The trajectories provide a dynamic map of molecular motion from which mean squared displacement and diffusion coefficients are calculated. To distinguish different mobility states, diffusion coefficients are plotted as a distribution and a threshold is set to at the inflection point between two peaks representing confined (low diffusion, blue) and non-confined (high diffusion, pink) motion. The proportion of molecules in each mobility state is then calculated to determine changes in nuclear dynamics across conditions.

Number and brightness (N&B). N&B analysis is conducted using confocal microscopy to acquire a time series of images of saturated labelled fluorescent molecules. The oligomeric state of the TFs is inferred by analysing fluctuations in fluorescence intensity at each pixel through time. These fluctuations are used to calculate brightness values, which scale with the number of fluorescent

molecules, in such a way that a dimer is approximately twice as bright as a monomer. Monomer calibration was assessed using a TF known to exist only in a monomeric state, allowing extrapolation to identify dimer and higher order oligomers.

Cross-raster image correlation spectroscopy (cRICS). Similar to N&B, cRICS involves acquiring a time series of images of saturated fluorescently labelled molecules. However, cRICS simultaneously captures two channels (different fluorophores) at high spatial resolution, ensuring that oversampling of the point spread function occurs. The RICS function computes spatial correlations of fluorescence fluctuations within each individual channel, revealing the diffusion behaviour of molecules in that channel. The cRICS function extends this by cross-correlating intensity fluctuations between the two channels, allowing detection of co-diffusing molecules. By comparing the diffusion coefficients obtained from the RICS (single channel) and cRICS (two channel), its possible to infer whether proteins are diffusing as monomers or as part of a complex, enabling quantification of interaction dynamics.

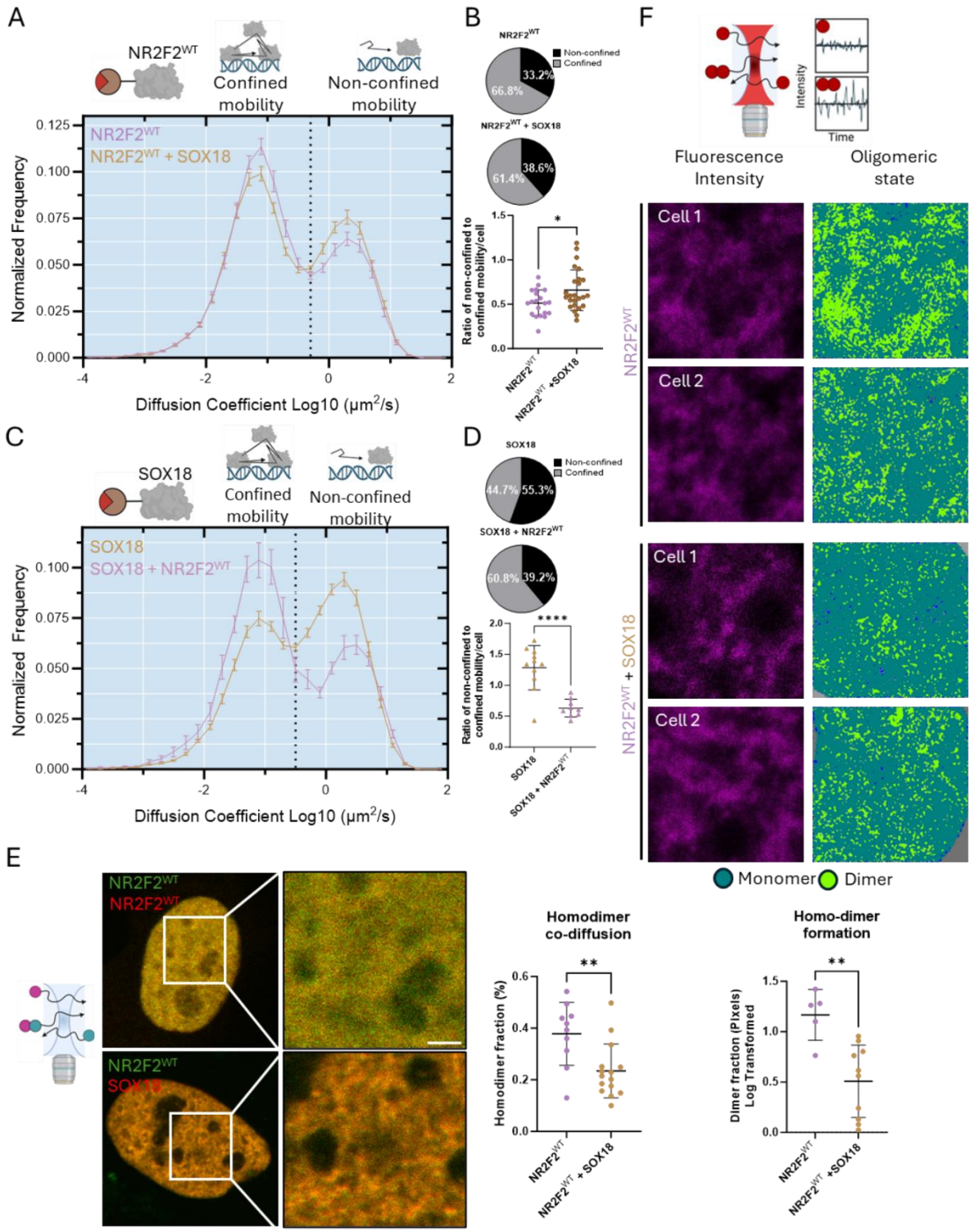

Fig 1: NR2F2 & SOX18 molecular interactions effect nuclear navigation. A Diffusion mobility graph from SMT comparing NR2F2^{WT} (purple) and NR2F2^{WT} + SOX18 (orange). **B** Pie charts represent the proportion of the population that falls into either confined mobility or non-confined mobility based on diffusion coefficient. SMT performed on NR2F2. Ratio of non-confined to confined molecules per cell from A. **C** Diffusion mobility graph from SMT comparing SOX18 (orange) and SOX18 + NR2F2^{WT} (purple). **D** Pie charts represent the proportion of the population that falls into either confined mobility or non-confined mobility based on diffusion coefficient. SMT performed on SOX18. Ratio of non-confined to confined molecules per cell from C. **E** Homo-dimer co-diffusion of NR2F2^{WT} or NR2F2^{WT}

+ SOX18 in the nucleus of cell. Nuclear regions of interest scale bar is 1um. **F** Homo-dimer formation measured by N&B. Fluorescent intensity of $NR2F2^{WT}$ (top row) and corresponding oligomeric state map (bottom) for either $NR2F2^{WT}$ or $NR2F2^{WT}$ + SOX18. For panel E n > 11 cells and for panel F n > 5 cell, statistical significance was determined by Welch's T-test, ** $p < 0.005$.

Interplay between SOX18 and NR2F2			
SMT (=TF mobility and dwell time)	**Observation**	**Biological interpretation**	**Fig**
$NR2F2^{WT}$ non-confined mobility in presence or absence of SOX18	$NR2F2^{WT}$+ SOX18: decreased proportion	$NR2F2^{WT}$ /SOX18 interplay leads to a more diffusive behavior of $NR2F2^{WT}$, possibly via sequestration away from chromatin or competitive binding	Fig 1A-B
$NR2F2^{WT}$ confined mobility (protein-protein or protein-chromatin interaction) in presence or absence of SOX18	$NR2F2^{WT}$ + SOX18: increased proportion		
SOX18 non-confined mobility (diffusing) in presence or absence of $NR2F2^{WT}$	SOX18+$NR2F2^{WT}$: decreased proportion	$NR2F2^{WT}$ stabilizes SOX18 binding leading to increased confined fraction and less diffusive behavior possibly via increase in SOX18 homodimer formation	Fig 1C-D
SOX18 confined mobility (protein-protein or protein-chromatin interaction) in presence of $NR2F2^{WT}$	SOX18+ $NR2F2^{WT}$: increased proportion		
N&B (=PPI, oligomeric status) and cRICS (co-diffusion)	**Biophysical Observation**	**Biological interpretation**	**Fig**
SOX18 / $NR2F2^{WT}$ heterodimer fraction relative to $NR2F2^{WT}$ only	$NR2F2^{WT}$ + SOX18: significantly decreased	SOX18 interferes with $NR2F2^{WT}$ homodimer formation	Fig 1E-F

Table 1: Summary of biophysical experiments and biological interpretations for NR2F2 and SOX18 interactions.

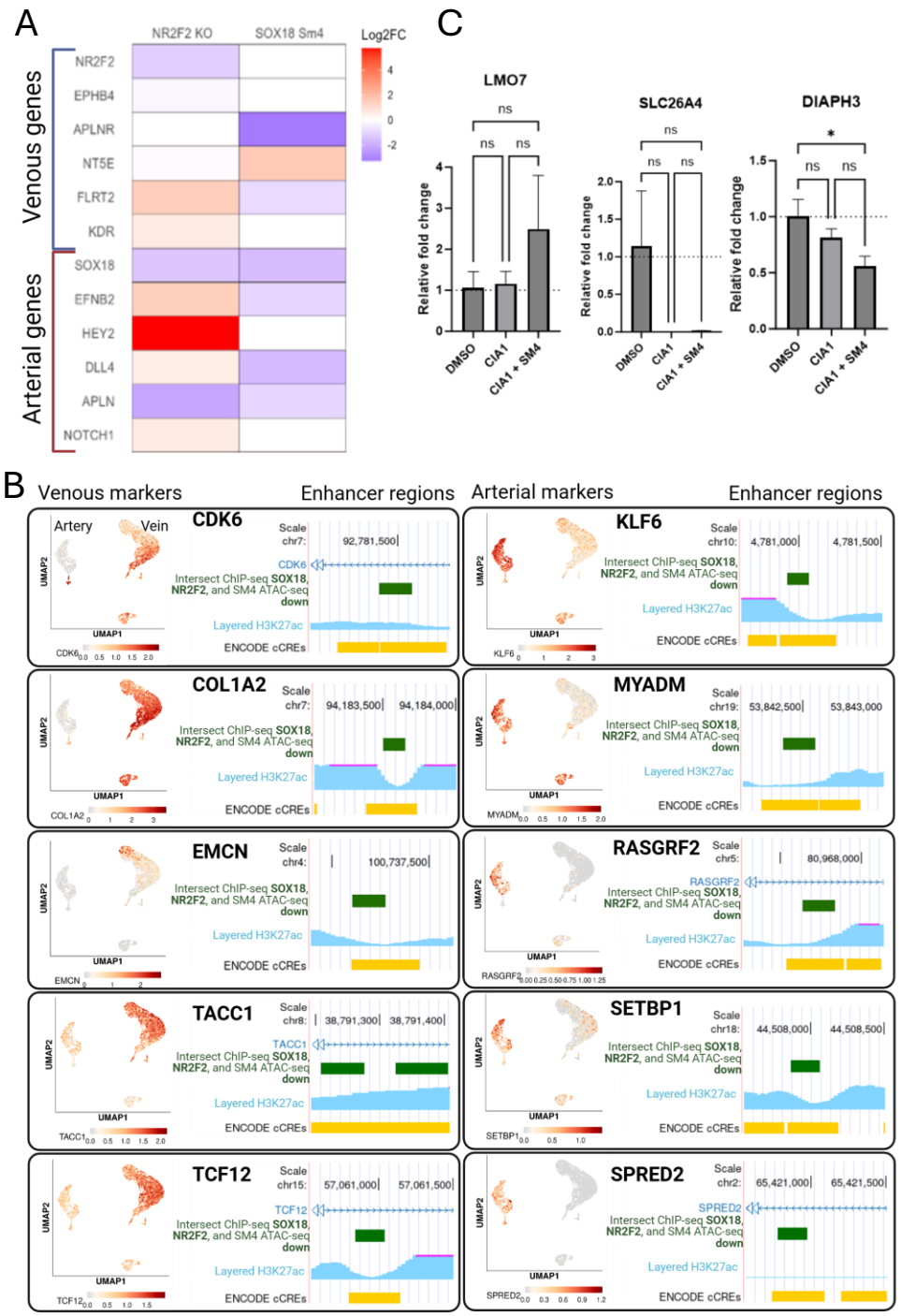

Supp Fig 3: NR2F2 and SOX18 co-regulate a set of genes that determine endothelial arterio-venous identity. **A** Expression level of a subset of genes commonly used to distinguish arterial and venous endothelial cells identity. Datasets are from publicly available scRNA-seq datasets (NR2F2 knockout (KO), Sissaoui et al., and SM4 treatment of SOX18, (Overman et al.) **B** Subset of genes that are identified as either venous or arterial based on scRNA-seq dataset (Ang et al.) correlated with two publicly available ChIP-seq datasets for either SOX18 (McCann et al.) and NR2F2 (Sissaoui et al.) intersected with an ATAC-seq dataset of HUVECs treated with SM4. **C** Relative gene expression of treated HUVECS measured by qPCR. For panel C (n = 3 repeats), statistical analysis was performed using one-way ANOVA, and significance between groups was determined using Tukey's multiple comparison post hoc test, * $p < 0.05$.

Gene	Peak summit coordinates (relative to TSS)
ABHD10	unnamed (-21638)
ACTR2	unnamed (+193040)
ADAMTS18	unnamed (-159060)
ADAMTS20	unnamed (+313335)
ADD3	unnamed (+74218)
ADGRG6	unnamed (+73680)
ADGRV1	unnamed (+329846)
ADK	unnamed (+352070)
AFF4	unnamed (+15894)
AKAP12	unnamed (-235230), unnamed (-172029)
AKR1E2	unnamed (-45262)
ANTXR1	unnamed (+240776)
APH1B	unnamed (-43661)
ARNTL2	unnamed (-40970)
ARRDC3	unnamed (+494716)
ATP23	unnamed (+312217)
ATXN1	unnamed (+415849)
BCAP29	unnamed (+14611)
BEND6	unnamed (-86431)
BET1	unnamed (-179205)
BMP2	unnamed (-205506)
BMPR1A	unnamed (-8600)
BMPR1B	unnamed (-506229)
BTG1	unnamed (+157575)
C1D	unnamed (+145579)
C2CD4A	unnamed (+57487)
C2CD4B	unnamed (+40819)
C2CD6	unnamed (-2315)
C3orf58	unnamed (+799765)
C9	unnamed (+3925)
CALCRL	unnamed (+128858)
CCDC89	unnamed (-39803)
CCKAR	unnamed (-78354)
CD180	unnamed (+133472)
CDK1	unnamed (+49796)
CDK17	unnamed (-45640)
CDK19	unnamed (+277995)
CDK6	unnamed (+52426)
CFAP54	unnamed (-43387)
CGNL1	unnamed (-315564)
CKMT2	unnamed (-265587)
CLVS2	unnamed (+551819)
COL1A2	unnamed (-210981)
COL8A1	unnamed (-667213)
CORO6	unnamed (-104242)
CTXN3	unnamed (+389791)
CYP20A1	unnamed (-132818)
DACH1	unnamed (+961923)
DCBLD2	unnamed (-69573)
DCN	unnamed (-805199)
DDI1	unnamed (-511251)
DEGS1	unnamed (+77013)
DGKD	unnamed (+132701)
DIAPH3	unnamed (+630101)
DLD	unnamed (+58089)
DLGAP1	unnamed (+707568)
DNER	unnamed (+259499)
DPH6	unnamed (+252767)
DST	unnamed (-16945)
DYNC2H1	unnamed (+415754)
EEA1	unnamed (-274177), unnamed (+159638)
EMCN	unnamed (-219098)
ENSG00000	unnamed (-74562)
EPAS1	unnamed (-229348)
ETAA1	unnamed (+520085)
EXOC6	unnamed (-32324)
FAM133B	unnamed (-191097)
FAM171A1	unnamed (+170260)
FAM198B	unnamed (+11418)
FAM84B	unnamed (-656879)
FASLG	unnamed (+238955)
FAT4	unnamed (+204144)
FBXL2	unnamed (+38592)
FER	unnamed (+357980)
FERMT1	unnamed (-438614)
FILIP1L	unnamed (-45319)
FNIP2	unnamed (+234001)
FRRS1	unnamed (+74373)
FUT10	unnamed (+842068)
FYB1	unnamed (-89978)
GALNT1	unnamed (+380766)
GFPT1	unnamed (+133300)
GMPR	unnamed (+107027)
GRIA2	unnamed (+940914)
GSN	unnamed (+22660)
HAS2	unnamed (-255283)
HHEX	unnamed (+126245)
HIVEP2	unnamed (+570756)
HMG20A	unnamed (+36858)
HMGA2	unnamed (+111844)
ICA1	unnamed (+400634)
ICE2	unnamed (-127075)
IFNE	unnamed (-67115)
IL7	unnamed (-528457)
ITPR2	unnamed (+154052)
KAT6B	unnamed (-323326)
KCNAB1	unnamed (+197013)
KCNMB2	unnamed (-295301)
KCTD12	unnamed (+373578)
KCTD18	unnamed (+103969)
KIAA0319L	unnamed (+51422)
KLF6	unnamed (-995717)
KLHL1	unnamed (-796810)
LAMA4	unnamed (+37243)
LAMB1	unnamed (+54196)
LDB2	unnamed (-119447)
LDB3	unnamed (+79601)
LEAP2	unnamed (+75418)
LINGO1	unnamed (+174958)
LLPH	unnamed (+194464)
LMO7	unnamed (+876154)
LRIG3	unnamed (+666728)
LRRC40	unnamed (+160570)
LRRC7	unnamed (+284875)
LSAMP	unnamed (-806917)
MAGEB5	unnamed (+572469)
MAML2	unnamed (+33917)
MAP2K1	unnamed (+19076)
Mar-07	unnamed (-1537)
MAST4	unnamed (+466966)
MBNL1	unnamed (-241910)
MKKS	unnamed (+80596)
MRPL17	unnamed (-12191)
MTAP	unnamed (-253115)
MTFR2	unnamed (+214477)
MTHFD1L	unnamed (+139090), unnamed (+202291)
MTMR2	unnamed (-384968)
MXI1	unnamed (-125425)
MYADM	unnamed (-26928)
MYC	unnamed (+7016)
NANOGP8	unnamed (-208291)
NDUFA4	unnamed (+782912)
NFIA	unnamed (+206059)
NFIB	unnamed (-59342)
NFKBIZ	unnamed (+329473)
NLRP12	unnamed (-18084)
NMT2	unnamed (-32106)
NRG1	unnamed (+82719)
NUDT4	unnamed (-174375)
NUDT7	unnamed (-128340)
NVL	unnamed (+70203)
OR1K1	unnamed (+19737)
OR2AG2	unnamed (+76384)
PALM2	unnamed (+247400)
PALMD	unnamed (+45477)
PDCD1LG2	unnamed (-684)
PDCL	unnamed (+8771)
PDE4D	unnamed (+330937)
PDE7B	unnamed (+184138)
PDLIM5	unnamed (+93593)
PEG10	unnamed (+41281)
PHLDB2	unnamed (+98217)
PID1	unnamed (-222974)
PJA2	unnamed (+304192)
PLEKHA2	unnamed (-110049), unnamed (-109925
PLEKHG7	unnamed (+33204)
PLSCR1	unnamed (+37920)
PLSCR2	unnamed (-37643), unnamed (+191162)
PLSCR4	unnamed (-26960)
POU5F1B	unnamed (-199018)
PPP1R9A	unnamed (-209986)
PPP3CA	unnamed (+610289)
PRICKLE1	unnamed (-648816)
PRKCE	unnamed (+416280)
PXN	unnamed (-25913)
QDPR	unnamed (+493978)
RAB3C	unnamed (+979821)
RAB8B	unnamed (+44424)
RAP1GAP	unnamed (-144916)
RAPGEF2	unnamed (-264598)
RASA2	unnamed (-829)
RASGRF2	unnamed (+7065)
RASGRP1	unnamed (-431706)
RCOR1	unnamed (+62663)
RERE	unnamed (+104741)
RHOBTB1	unnamed (+115997)
RORA	unnamed (+21243)
RPA3	unnamed (-143040)
RPIA	unnamed (+45928)
RPRD1A	unnamed (+32250)
SEMA6D	unnamed (-252013)
Sep-11	unnamed (-500278)
SETBP1	unnamed (-172934)
SGO1	unnamed (-70064)
SHROOM3	unnamed (+14459)
SIRT4	unnamed (-10637)
SLC12A2	unnamed (-44931)
SLC22A16	unnamed (-60680)
SLC26A4	unnamed (-65265)
SLC38A2	unnamed (-57589)
SLC38A4	unnamed (+395541)
SLC45A1	unnamed (+394898)
SMCO2	unnamed (-4319)
SNAP25	unnamed (+134796)
SNAPC5	unnamed (+91920)
SNCA	unnamed (+288303)
SNRPE	unnamed (+27452)
SNTB2	unnamed (+37991)
SNX9	unnamed (-287268)
SOX13	unnamed (-184537)
SPATS2L	unnamed (+97144)
SPRED2	unnamed (+11300)
SS18	unnamed (+572392)
SSH2	unnamed (+202952)
SSPN	unnamed (+483650)
SSR3	unnamed (+237588)
STAT1	unnamed (-17197)
STAT4	unnamed (+119813)
STK38L	unnamed (+47910)
STMN2	unnamed (-277172)
STOM	unnamed (+47752)
SUCNR1	unnamed (+152487)
SYTL2	unnamed (+85049)
TACC1	unnamed (+4038), unnamed (+4162)
TBC1D19	unnamed (-15100)
TBC1D23	unnamed (-101180)
TCF12	unnamed (+142318)
TGIF1	unnamed (+296090)
THBS1	unnamed (-584581)
TIGD2	unnamed (+438512)
TLE3	unnamed (-592919)
TM2D1	unnamed (+437220)
TMEM2	unnamed (+623377)
TNFSF18	unnamed (+152990)
TRAF3	unnamed (-122152)
TRDN	unnamed (+89303)
TRPM3	unnamed (-23909)
TTC26	unnamed (+20234)
TUBE1	unnamed (-129959)
TXN	unnamed (+228801)
UACA	unnamed (+72498)
UBE2R2	unnamed (-2551)
UBN2	unnamed (-77473)
UBP1	unnamed (+124364)
USP40	unnamed (+78382)
USP48	unnamed (+18649)
UTRN	unnamed (+58180)
WDR12	unnamed (-193896)
ZDHHC14	unnamed (+154863)
ZDHHC21	unnamed (+320462)
ZHX2	unnamed (-884721)
ZMYM4	unnamed (+237024)
ZNF521	unnamed (-166081)
ZPLD1	unnamed (-256028)
ZSWIM2	unnamed (-470432)

Supp Table 1: Peak to gene analysis of assigned enhancers relative to TSS from intersected peaks with ATAC-seq and ChIP-seq datasets.

Gene	Cell type
ARHGEF37	venous
ATG16L2	venous
BBS12	venous
CHST2	venous
CMSS1	pre venous/ venous/ arterial
DCBLD2	pre arterial pre venous
DDR2	pre venous
DEK	pre venous/ arterial
DIAPH3	pre venous
DUSP4	pre venous/ arterial
EDN1	arterial / venous
ERRFI1	pre venous/ arterial
FAM171A1	arterial / venous
FBXO5	pre arterial pre venous
FHL2	pre arterial
FKBP5	venous
GALNT1	pan endothelial
GATA6	pre venous
GIMAP4	venous
HIST1H2AE	venous
HIST1H2BB	low
HIST1H2BG	low
HIST1H2BJ	venous
HIST1H3C	low venous
HIST1H4E	venous
HIST1H4H	venous/artery
HTR1B	pre venous
IL20RB	low
KCNAB2	low
KIF20B	pre arterial pre venous
LMO7	pre venous low
MBNL1	venous
MEF2C	venous
MMP10	low
MN1	pre venous / venous

Gene	Cell type
MXI1	venous
NRP1	arterial/ venous
NTN4	pre venous
OGT	venous
OTOGL	low
PDE3A	pre venous
PDLIM3	pre venous
PIK3R3	pre venous / venous
PKN2	pre venous / venous
PPIB	pan endothelial high
RALGPS2	pre arterial / pre venous / venous
RFC3	pre venous / venous
RGCC	arterial / venous
SCFD2	venous
SERBP1	venous
SESN1	venous
SHCBP1	arterial / pre venous
SLC1A4	arterial
SLC7A11	arterial / pre venous
SLC26A4	venous
SLC38A1	arterial / venous
SLC45A1	venous
SPRY1	arterial / hemogenic
STC1	pre arterial
STC2	arterial
SYNE1	pre venous/ venous
TAPT1	venous
THBS1	pre arterial pre venous
TMEM47	pre venous
TMEM170E	venous
TNRC6A	venous/ arterial
TRAF3IP2	arterial / venous
TUBE1	arterial venous
YAE1D1	pre venous

Supp Table 2: Subset of genes from Supp Table 1 that have arterial or venous specific profiles.

A

Gene	HUVEC (log2 fold)	Gene	HUVEC (log2 fold)
STC2	3.11	RALGPS2	0.03
KLF4	2.29	FAM171A1	0.01
VEGFA	2.15	PDLIM3	0.00
SLC1A4	2.09	TNRC6A	0.00
SLC7A11	1.77	HIST1H3E	-0.02
LMO7	1.57	KCNAB2	-0.03
ERRFI1	1.47	MN1	-0.05
SLC38A1	1.28	TMEM170B	-0.08
TUBE1	1.24	YAE1D1	-0.10
DDR2	1.08	GIMAP4	-0.10
STC1	0.91	HIST1H2AE	-0.18
FHL2	0.87	EDN1	-0.22
DCBLD2	0.86	FKBP5	-0.24
SYNE1	0.71	PDE3A	-0.26
OGT	0.71	THBS1	-0.28
TMEM47	0.68	GATA6	-0.28
BBS12	0.60	GALNT1	-0.30
ATG16L2	0.50	FBXO5	-0.33
MXI1	0.43	SCFD2	-0.40
CMSS1	0.41	PIK3R3	-0.51
DEK	0.38	HTR1B	-0.57
TAPT1	0.37	DIAPH3	-0.57
CHST2	0.34	HIST1H2BG	-0.63
DUSP4	0.32	RFC3	-0.66
ARHGEF37	0.28	HIST1H4H	-0.68
MEF2C	0.27	KIF20B	-0.81
RGCC	0.24	HIST1H2BB	-0.83
MBNL1	0.22	HIST1H2BJ	-0.83
NTN4	0.21	SHCBP1	-1.14
SPRY1	0.20	HIST1H3C	
PKN2	0.19	IL20RB	
NRP1	0.17	OTOGL	
SESN1	0.16	SLC26A4	
SERBP1	0.16	MMP7	
MMP10	0.13	VCAM1	
NOTCH1	0.08		
TRAF3IP2	0.07		
IL33	0.06		
HIST1H4E	0.06		
SLC45A1	0.06		
PPIB	0.04		

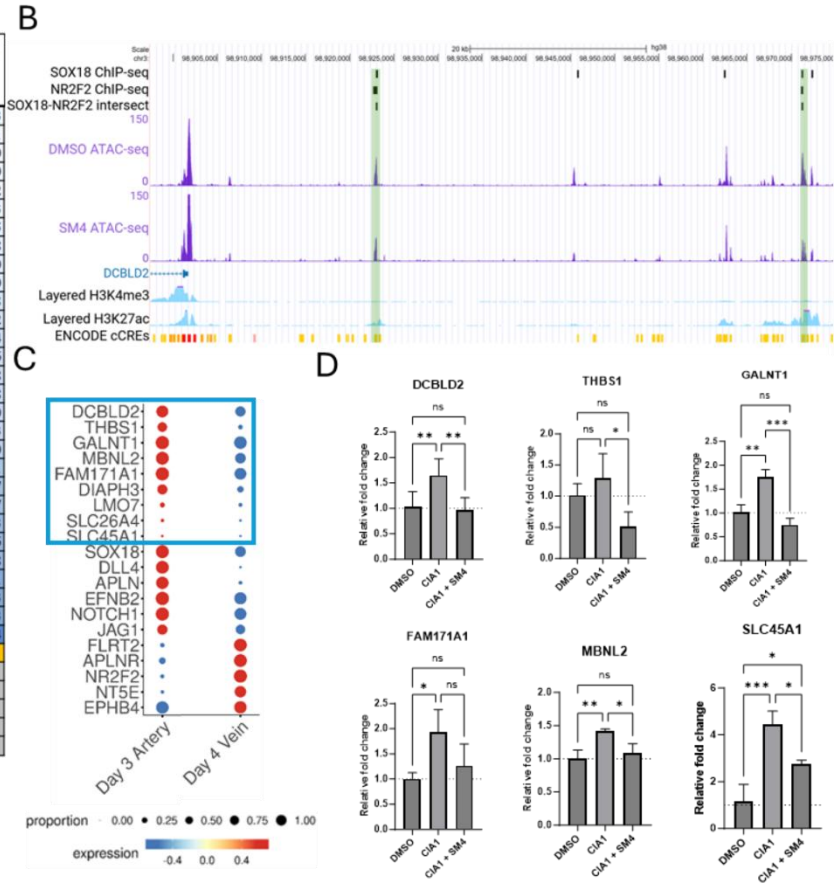

Fig 2: NR2F2 & SOX18 antagonistic co-regulation during venous differentiation. A Relative expression of a subset of genes from HUVECs treated with SM4 and measured by qPCR from Supp Table 2. Genes highlighted in yellow are the random subset of genes identified. **B** Layering of SOX18, NR2F2 ChIP-seq datasets from Sissaoui et al. (NR2F2) and Overman et al. (SOX18) (black bars), with ATAC-seq (purple), histone marks (light blue), and ENCODE cis regulatory elements map (red/orange/yellow) upstream of the DCBLD2 gene locus in HUVECs. Green boxes denote co-binding locations at distal enhancer regions by both NR2F2 and SOX18. **C** Proportion and expression of known arterio-venous identity markers. Blue box denotes a subset of genes that are found to be regulated by both NR2F2 and SOX18. Data is from Ang et al. **D** Relative gene expression of the subset of genes from panel A. HUVECs were treated with DMSO, CIA1, or CIA1 + SM4. For panel I (n = 3 repeats), statistical analysis was performed using one-way ANOVA, and significance between groups was determined using Tukey's multiple comparison post hoc test, * $p < 0.05$, ** $p < 0.005$, *** $p < 000.5$, **** $p < 0.0001$.

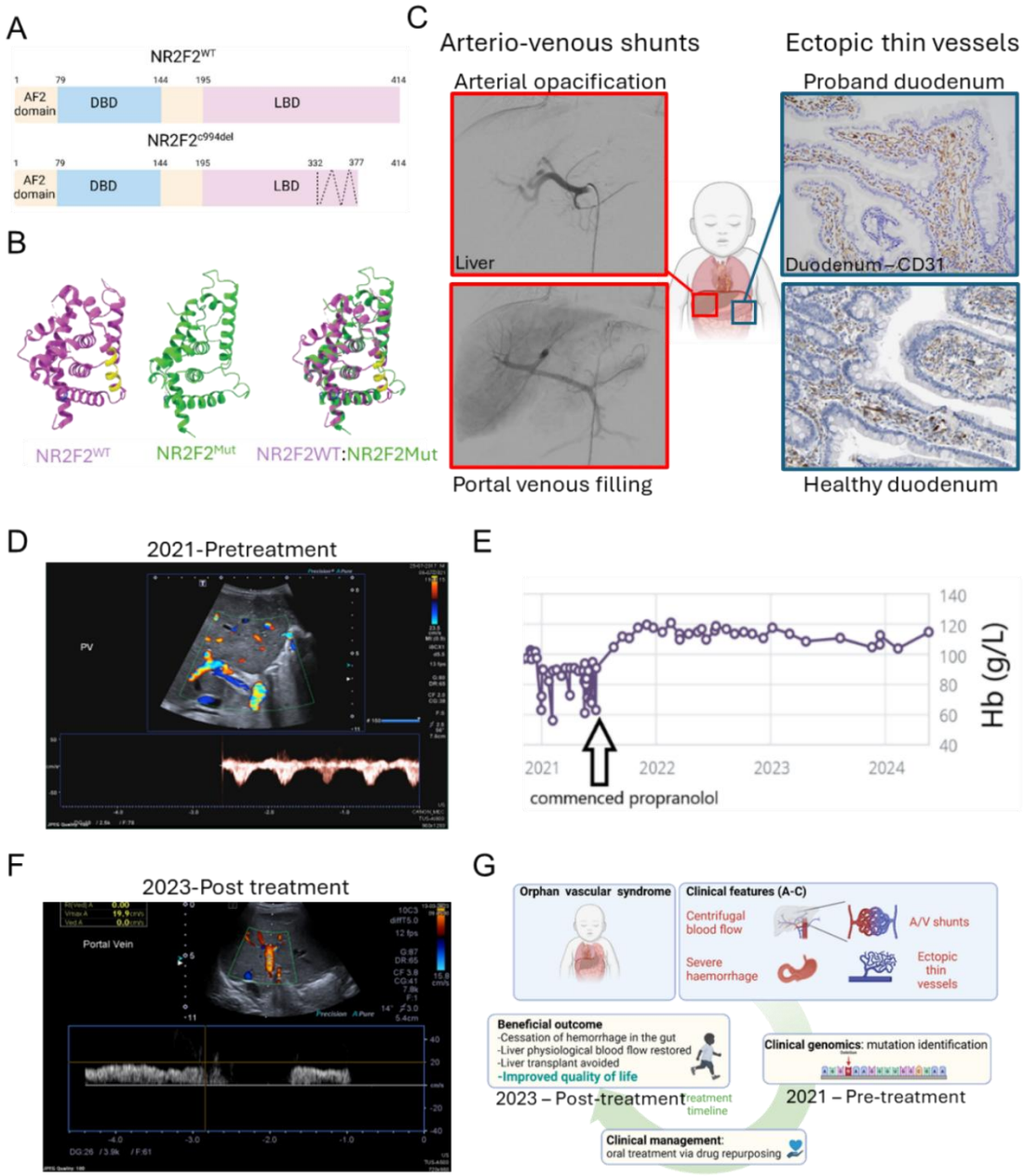

Fig 3: A *de novo* NR2F2 pathogenic variant causes an arterio-venous disorder that is responsive to SOX18 inhibition with propranolol. A Schematic representation of $NR2F2^{WT}$ and $NR2F2^{Mut}$. **B** Modeled structure of the LBD of $NR2F2^{WT}$ (purple) and $NR2F2^{Mut}$ (green). The crystal structure of the LBD was previously produced by Kruse et al. This comparison uncovers conformation difference (yellow). **C** Images from the proband's hepatic angiography. Arterial opacification (top, red boarder) and subsequent portal venous filling (bottom, red boarder) showing diffuse arterioportal shunting. Tissue section of duodenum (H&E and counter-stained for CD31), reveals an increased number of thin-walled ectopic vessels in the proband (top, blue boarder) and healthy duodenum from a 50 year old male (bottom, blue boarder). Healthy duodenum image is the Human Atlas. **D** Doppler ultra-sound of the portal vein prior to propranolol treatment shows hepatofugal (reversed) flow in the portal vein consistent with portal hypertension. **E** Clinical tracking of hemoglobin levels prior and post propranolol treatment. **F** Doppler ultra-sound of portal vein post propranolol treatment showing restoration of physiological blood flow (hepatopetal). **G** Treatment and recovery timeline; including identification of clinical features, identification of NR2F2 variant, followed by propranolol treatment and successful pharmacological management of the condition.

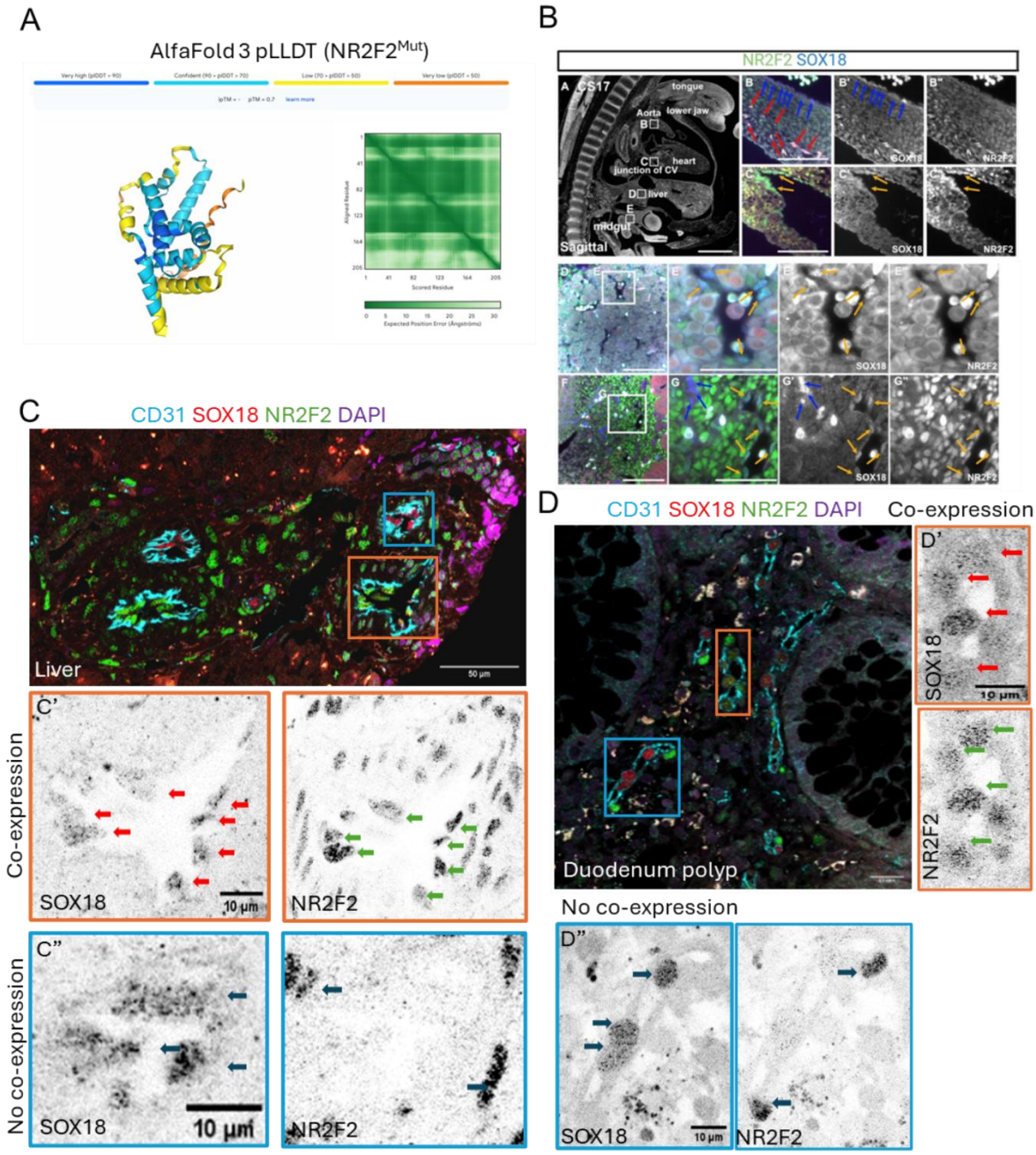

Supp Fig 4: NR2F2 and SOX18 are co-expressed in human ECs during embryogenesis and in the proband tissues. A The predicted local distance difference tests (pLDDT) for the LBD of NR2F2^{Mut}. **B** Immunostaining of NR2F2 (green) and SOX18 (blue) in sagittal sections from a CS17 embryo (A-D'''). The immunostaining shows co-expression of NR2F2 and SOX18 in endothelial cells during human development. **C-C**" and **D-D**" Sections of proband liver (C) and duodenum (D) stained for CD31 (cyan), SOX18 (red arrows), NR2F2 (green arrows), and DAPI (purple). Orange and blue boxes denote zoomed in regions of individual vessels. Orange box represents vessel that shows cells co-expressing both NR2F2 and SOX18 in the same nucleus, whereas the gold box is a vessel with cells either expressing NR2F2 or SOX18. Scale bar = 50µm (C-D) and 10 µm (C'''-D''').

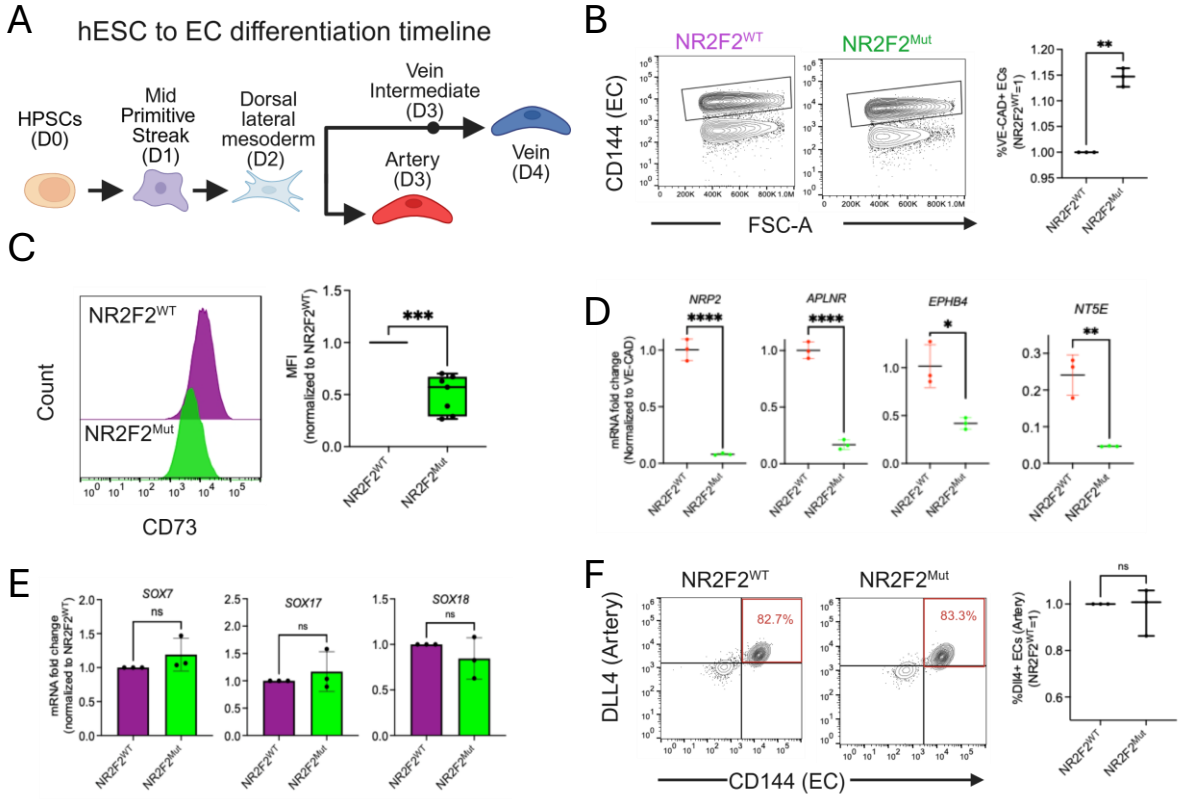

Fig 4: Patient's variant impairs differentiation of hESC to venous endothelial cells. A Representative timeline of hESC to EC timeline. **B** Flow cytometry analysis of VE-Cadherin (pan-EC) positive ECs at day 4 of differentiation. WT (purple) Mut (green), Quantification of VE-Cadherin. **C** Histogram plots of CD73 expression in day 4 venous ECs derived from $NR2F2^{WT}$ and $NR2F2^{c994del}$ H1-hESC and corresponding quantification of median fluorescence intensity (MFI). **D,E** qPCR performed on day 4 venous ECs. **F** Flow cytometry analysis of artery ECs at day 4 and corresponding quantification of % DLL4+ CD144+ endothelial cells. Each data point represents independent repeats of n≥3. Statistical significance was determined by Welch's T-test, * $p < 0.05$, ** $p < 0.005$, *** $p < 0.0005$, **** $p < 0.0001$.

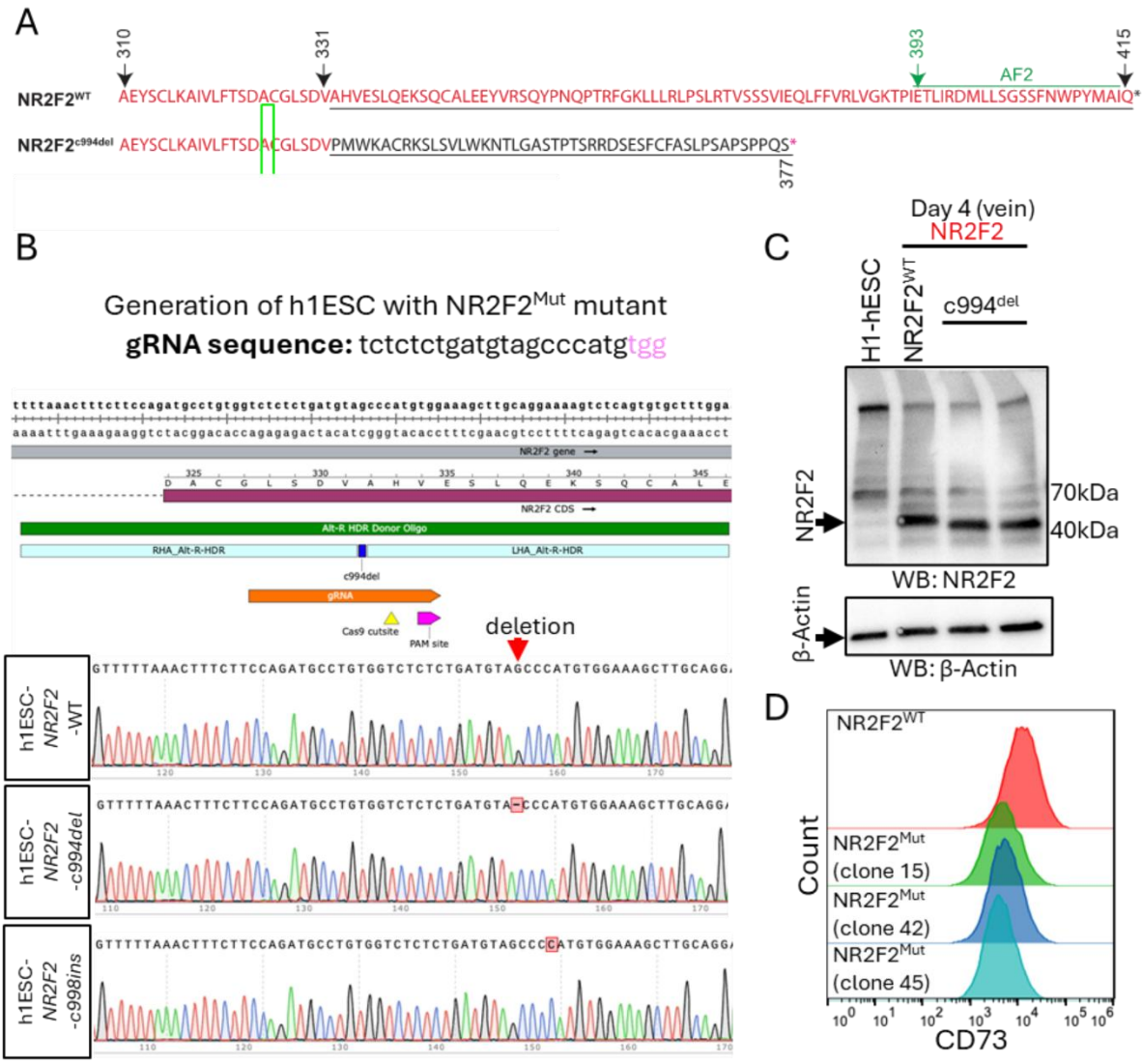

Supp Fig 5: Generation of hESC with NR2F2^{Mut} variant. A Amino acid sequence comparison of NR2F2^{WT} and NR2F2^{Mut}, NR2F2^{c998ins}, an unrelated CRISPR modified cells used as control. **B** Generation of H1-hESC mutant clones harboring the NR2F2^{Mut} variant and an unrelated clone NR2F2^{c998ins}. **C** Western blot showing NR2F2^{Mut} protein expression levels compared to wild type in hESC derived venous cells. **D** Histogram plots of CD73 expression on day four venous endothelial cells derived from different CRISPR- clones of NR2F2^{Mut} h1ESCs.

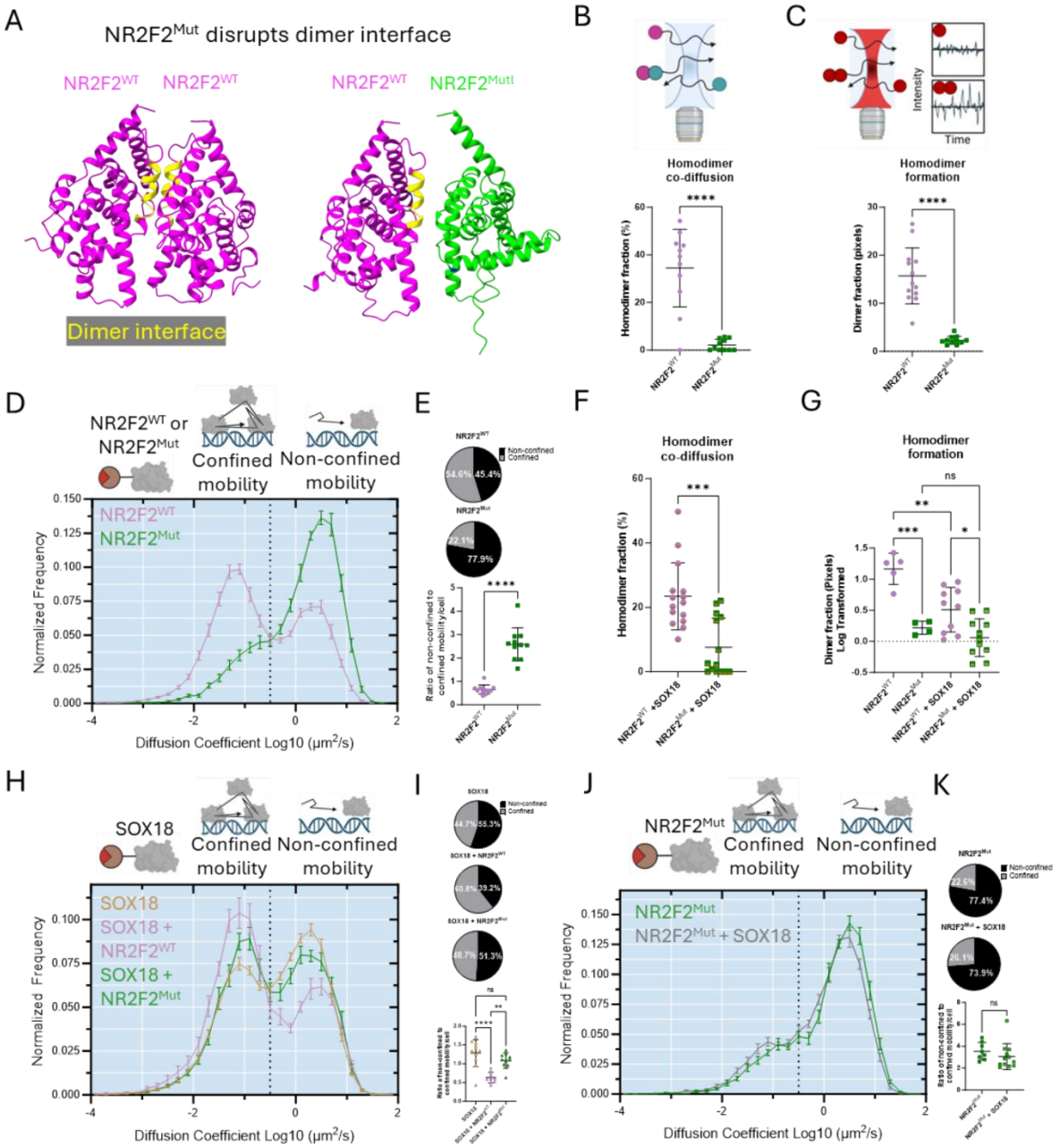

Fig 5: NR2F2^{Mut} variant shows altered molecular behavior and unbalances SOX18 activity. A Modeled dimerization of the LBD of NR2F2^{WT} (purple) and NR2F2^{c994del} (green), dimerization domains (yellow). NR2F2^{WT} or NR2F2^{Mut} measured by cRICS to assess homo-dimer co-diffusion. **B, C** NR2F2^{WT} or NR2F2^{Mut} measured by cRICS (B) and N&B (C) to assess homo-dimer diffusion and formation. **D** Diffusion mobility graph from SMT comparing NR2F2^{WT} and NR2F2^{Mut}. **E** Pie charts represent the proportion of the population that falls into either confined mobility or non-confined mobility based on diffusion coefficient. Ratio of non-confined to confined molecules per cell from D. **F, G** Hetero-dimer co-diffusion of NR2F2^{WT} + SOX18 or NR2F2^{Mut} + SOX18 measured by cRICS (F) and N&B (G). **H** Diffusion mobility graph from SMT comparing SOX18 (orange), SOX18 + NR2F2^{WT} (purple), and SOX18 + NR2F2^{Mut} (green). **I** Pie charts represent the proportion of the population that falls into either confined mobility or non-confined mobility based on diffusion coefficient. SMT performed on SOX18. Ratio of non-confined to confined molecules per cell from H. **J** Diffusion mobility graph from SMT comparing NR2F2^{Mut} (green) and NR2F2^{c994del} + SOX18 (grey). **K** Pie charts represent the proportion of the population that falls into either confined mobility or non-confined mobility based on diffusion coefficient. SMT performed on NR2F2. Ratio of non-confined to confined

molecules per cell from J. For panels B, C, E, F, and K; n > 12 cells, statistical analysis was performed using Welch's T-test, * $p < 0.05$, ** $p < 0.005$, *** $p < 000.5$, **** $p < 0.0001$. For panels G and I n > 5 cells, statistical analysis was performed using one-way ANOVA, and significance between groups was determined using Tukey's multiple comparison post hoc test, * $p < 0.05$, ** $p < 0.005$, *** $p < 000.5$, **** $p < 0.0001$.

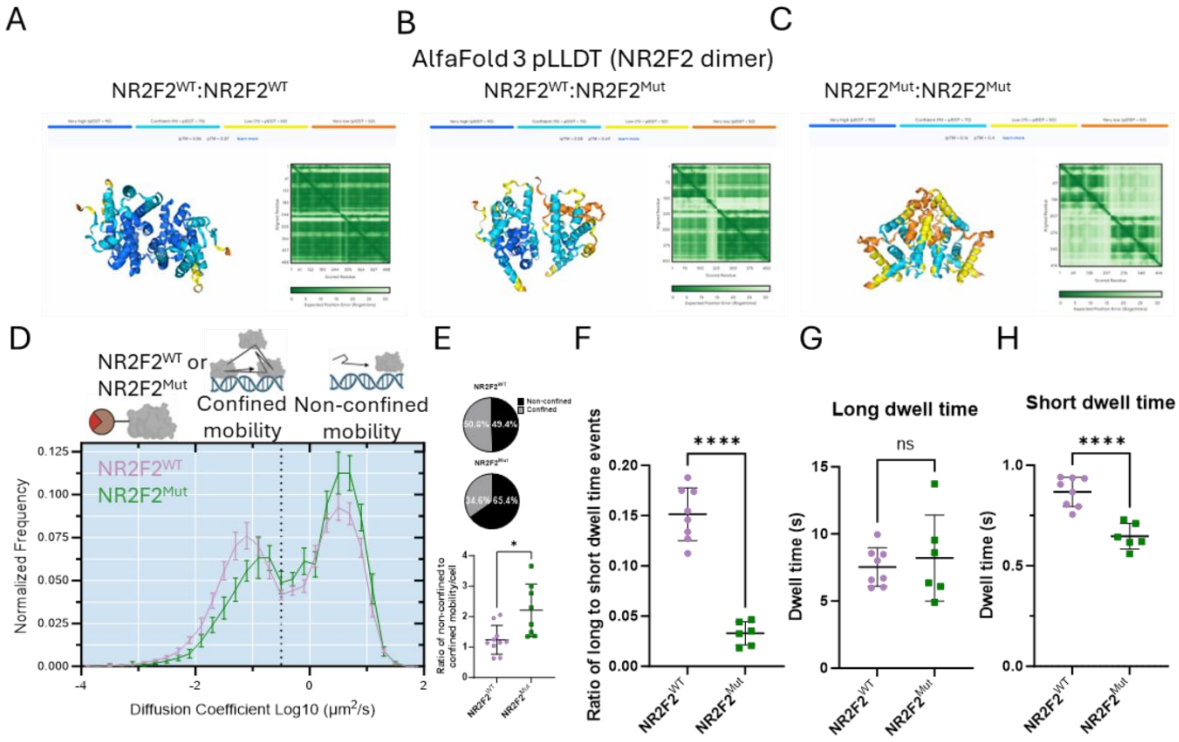

Supp Fig 6: *In silico* modeling of NR2F2 LBD of variant shows loss of interaction. A-C The predicted local distance difference tests (pLDDT) for dimerization of LBD NR2F2^{WT} (A) and dimerization of NR2F2^{WT}, NR2F2^{Mut} (B) and dimerization of NR2F2^{Mut} (note low confidence in the structure). **D** Diffusion mobility graph from SMT comparing NR2F2^{WT} and NR2F2^{Mut} in HUVECs. **E** Pie charts represent the proportion of the population that falls into either confined mobility or non-confined mobility based on diffusion coefficient. Ratio of non-confined to confined molecules per cell from C. **F-H**) Temporal occupancy characteristics. E) Ratio of long to short dwell times, F) long dwell time, and G) short dwell times. For panels D-G, n > 6 cells, statistical significance was determined by Welch's T-test, * $p < 0.05$, **** $p < 0.0001$.

Interference mechanism caused by the variant			
N&B (=PPI, oligomeric status) and cRICS (co-diffusion)	**Biophysical Observation**	**Biological interpretation**	**Fig**
$NR2F2^{WT}$ homodimer formation and co-diffusion compared to $NR2F2^{Mut}$	$NR2F2^{Mut}$: significantly decreased	c994del does not form homodimers	Fig. 5B,C
$NR2F2^{WT}$ homodimer co-diffusion compared to $NR2F2^{Mut}$ in the presence of SOX18	$NR2F2^{Mut}$: significantly decreased	The presence of SOX18 does not affect homodimer co-diffusion	Fig. 5F
$NR2F2^{WT}$ homodimer formation compared to $NR2F2^{Mut}$ in the presence of SOX18	$NR2F2^{Mut}$: significantly decreased	The presence of SOX18 does not affect homodimer formation	Fig. 5G
SMT (=TF mobility and dwell time)	**Biophysical Observation**	**Biological interpretation**	**Fig**
$NR2F2^{WT}$ non-confined mobility (diffusing) compared to $NR2F2^{Mut}$	$NR2F2^{WT}$: decreased proportion	$NR2F2^{WT}$ can interact with chromatin and other proteins whereas $NR2F2^{Mut}$ is unable to do so	Fig. 5D,E
$NR2F2^{WT}$ confined mobility (protein-protein or protein-chromatin interaction) in presence of $NR2F2^{Mut}$	$NR2F2^{WT}$: increased proportion		
SOX18 non-confined mobility (diffusing) in presence or absence of $NR2F2^{WT}$	SOX18 + $NR2F2^{WT}$: decreased proportion	$NR2F2^{WT}$ stabilizes SOX18 binding leading to increased confined fraction and less diffusive behavior possibly via increase in SOX18 homodimer formation, but does not influence $NR2F2^{Mut}$	Fig. 5H,I
SOX18 confined mobility (protein-protein or protein-chromatin interaction) in presence of $NR2F2^{WT}$	SOX18 + $NR2F2^{WT}$: increased proportion		
SOX18 non-confined mobility (diffusing) in presence or absence of $NR2F2^{Mut}$	SOX18 + $NR2F2^{Mut}$: no change		Fig. 5H,I
SOX18 confined mobility (protein-protein or protein-chromatin interaction) in presence of $NR2F2^{Mut}$	SOX18 + $NR2F2^{Mut}$: no change		
$NR2F2^{Mut}$ non-confined mobility diffusing) relative to $NR2F2^{Mut}$ + SOX18	$NR2F2^{Mut}$+ SOX18: no change = no interaction with SOX18	Majority of c994del molecules diffuse rather than interact = failure to efficiently select target genome location	Fig. 5J,K
$NR2F2^{Mut}$ confined mobility (protein-protein or protein-chromatin interaction) relative to $NR2F2^{Mut}$ + SOX18	$NR2F2^{Mut}$ + SOX18: no change = no interaction with SOX18		

Table 2: Summary of biophysical experiments and biological interpretations of NR2F2 and SOX18 interactions.

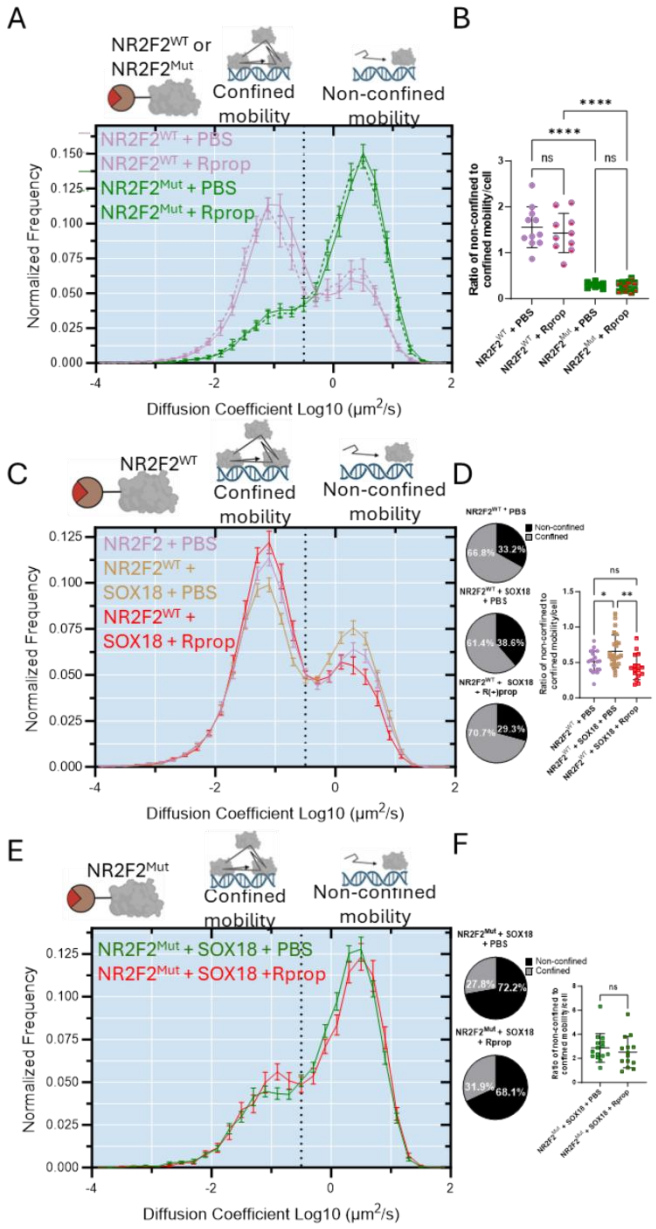

Fig 6: NR2F2^{Mut} molecular rescue with R(+)propranolol treatment is SOX18-dependent. A Diffusion mobility graph from SMT comparing NR2F2^{WT} + PBS (purple), NR2F2^{WT} + Rprop (purple, hashed), NR2F2^{Mut} + PBS (green), and NR2F2^{Mut} + Rprop (green, hashed). SMT performed on NR2F2. **B** Ratio of non-confined to confined molecules per cell from A. **C** SMT performed on NR2F2. Diffusion mobility graph from SMT comparing NR2F2^{WT} + PBS (purple), NR2F2^{WT} + SOX18 + PBS (orange), and NR2F2^{WT} + SOX18 + R(+)prop (red). **D** Pie charts represent the proportion of the population that falls into either confined mobility or non-confined mobility based on diffusion coefficient. Ratio of non-confined to confined molecules per cell from C. **E** Diffusion mobility graph from SMT comparing NR2F2^{c994del} + SOX18 + PBS (grey), and NR2F2^{c994del} + SOX18 + Rprop (red). **F** Pie charts represent the proportion of the population that falls into either confined mobility or non-confined mobility based on diffusion coefficient. SMT performed on NR2F2. Ratio of non-confined to confined molecules per cell from E. For panels B and D; n > 8 cells, for panel F; n > 14 cells, statistical significance was determined by Welch's T-test. Statistical analysis was performed using one-way ANOVA, and significance between groups was determined using Tukey's multiple comparison post hoc test, * $p < 0.05$, ** $p < 0.005$, **** $p < 0.0001$.

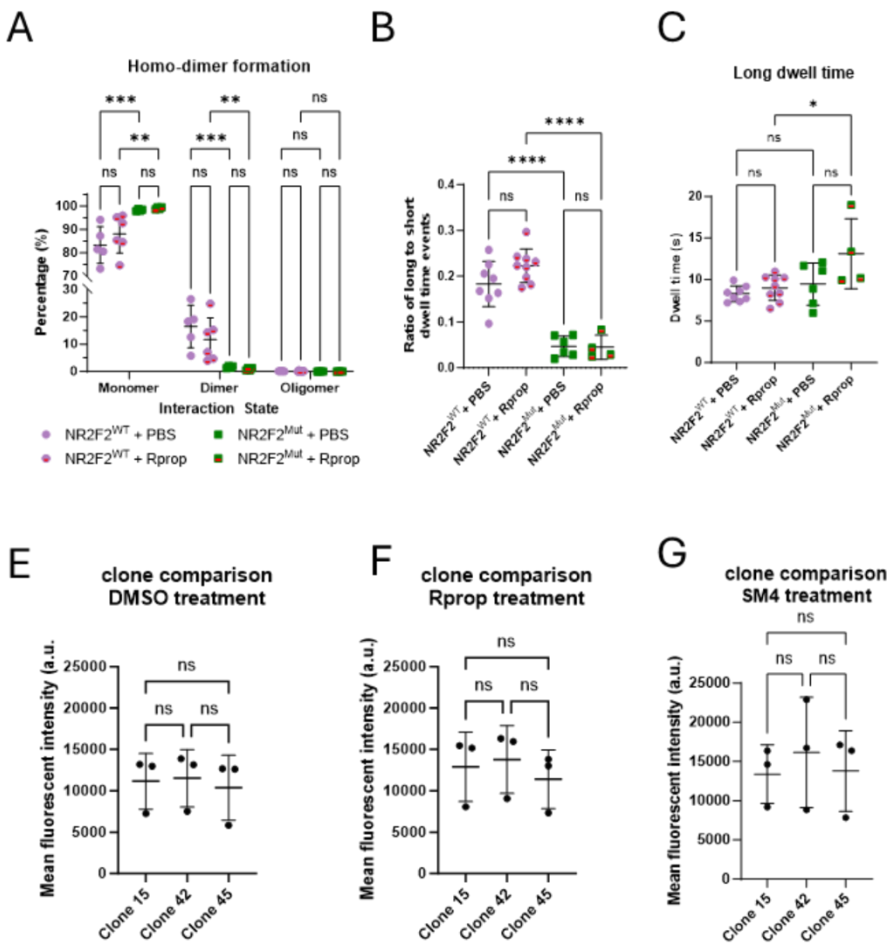

Supp Fig 7: Dimer formation and temporal occupancy are not affected by propranolol treatment and hESC NR2F2^{Mut} clones react in a similar way to SOX18 inhibition. A Monomer, dimer, and oligomeric states measured by N&B. **B-D** Temporal occupancy characteristics. D Ratio of long to short dwell times, E long dwell time, and F short dwell times. **E-G** CD73 expression on NR2F2^{Mut} cells treated with either R(+)propranolol or SOX18. Statistical analysis was performed using a two-way ANOVA, statistical significance between groups was determined using Tukey's multiple comparison post hoc test (A), a one-way ANOVA (B-D), statistical significance between groups was determined using Tukey's multiple comparison post hoc test and a Kruskal-Wallis test (E-G), statistical significance between groups was determined using Dunn's multiple comparison test , * $p < 0.05$, ** $p < 0.005$, *** $p < 0.0005$, and **** $p < 0.0001$.

Drug mode of action			
N&B (=PPI, oligomeric status) and cRICS (co-diffusion)	**Biophysical Observation**	**Biological interpretation**	**Fig**
$NR2F2^{WT}$ + PBS homodimer fraction compared to $NR2F2^{WT}$ + R-propranolol	$NR2F2^{WT}$ + R(+)propranolol: no change	R-propranolol does not affect $NR2F2^{WT}$ dimer formation	Supp Fig. 7A
$NR2F2^{WT}$ homodimer fraction relative to $NR2F2^{Mut}$ + R-propranolol	$NR2F2^{Mut}$ + R(+)propranolol: no change	R-propranolol does not affect $NR2F2^{Mut}$ oligomeric status	Supp Fig. 7A
SMT (=TF mobility and dwell time)	**Biophysical Observation**	**Biological interuption**	**Fig**
non-confined mobility (diffusing) of $NR2F2^{WT}$ or $NR2F2^{Mut}$ in presence or absence of R(+)propranolol	no change caused by drug treatment	R(+)propranolol does not affect $NR2F2^{WT}$ or variant mobility	Fig. 6A,B
confined mobility (diffusing) of $NR2F2^{WT}$ or $NR2F2^{Mut}$ in presence or absence of R(+)propranolol	no change caused by drug treatment		
$NR2F2^{WT}$ non-confined mobility (diffusing) in presence or absence of SOX18 with or without R(+)propranolol	Adding SOX18 leads to increased NR2F2 diffusion, effects that are counteracted by R(+)propranolol	R(+)propranolol rescues $NR2F2^{WT}$ changes of behavior that are caused by SOX18	Fig. 6C,D
$NR2F2^{WT}$ confined mobility (diffusing) in presence or absence of SOX18 with or without R(+)propranolol	Adding SOX18 leads to decreased NR2F2 bound fraction, effects that are counteracted by R(+)propranolol		
$NR2F2^{Mut}$ non-confined mobility (diffusing) in presence of SOX18 with or without R(+)propranolol treatment	$NR2F2^{Mut}$ + SOX18 +/- R(+)propranolol: no change	Inhibition of SOX18 does not impact variant mobility	Fig. 6E,F
$NR2F2^{Mut}$ confined mobility (protein-protein or protein-chromatin interaction) in presence of SOX18 with or without R(+)propranolol treatment	$NR2F2^{Mut}$ + SOX18 +/- R(+)propranolol: no change		

Table 3: Summary of biophysical experiments and biological interpretations investigating drugs effect on NR2F2 and SOX18.

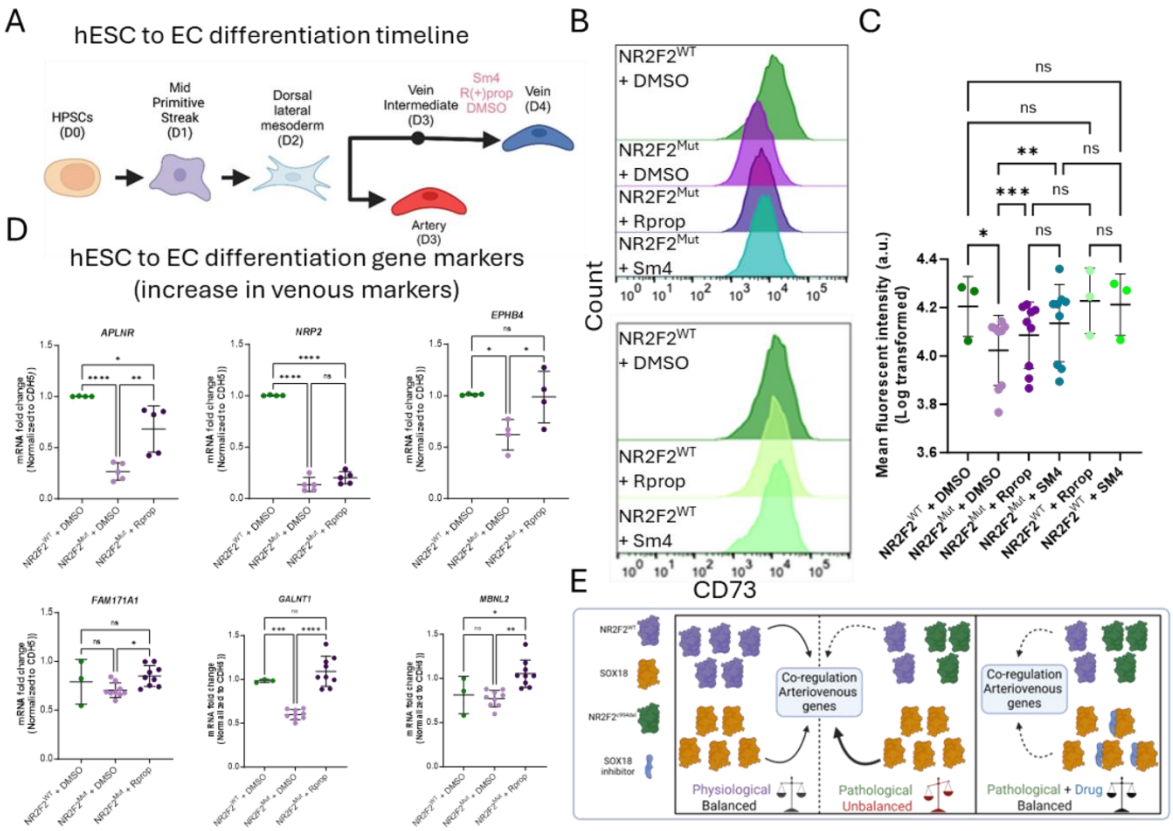

Fig 7: Both SOX18 small molecule inhibitor and Propranolol rescue NR2F2^{Mut}-induced venous differentiation defects. A Schematic of hESC to EC differentiation timeline with drug treatment. **B** Histogram plots of venous derived populations and corresponding quantification of MFI. An increase of the CD73 expression occurs in the presence of SOX18 blockers despite the NR2F2 mutation. **C** Comparison of CD73 expression. The three clones carrying the mutant version of NR2F2 are pooled. **D** Relative gene expression measured by qPCR from day four venous cells. **E** Model of the proposed molecular mechanism underlying the NR2F2^{c994del} rescue. Under physiological conditions in venous cells, NR2F2 and SOX18 are co-expressed at a specific ratio. This ratio allows for an antagonistic co-regulation of arteriovenous markers in vein ECs that is essential to maintain venous identity. In the proband's scenario NR2F2 heterozygous mutation alters the proper ratio between NR2F2^{WT} and SOX18 that then becomes unbalanced in favor of SOX18 activity, leading to an upregulation of arterial markers and a perturbation of venous identity. Treatment with a SOX18 inhibitor enables the restoration of balance between SOX18 and NR2F2 activity, allowing a smaller proportion of both TF populations to function properly at physiological levels. Panel C ($n > 3$ repeats of 10000 cell/cell line), statistical analysis was performed using a mixed-effects analysis, with the Geisser-Greenhouse correction, and Tukey's multiple comparison test, * $p < 0.03$, ** $p < 0.002$, *** $p < 0.0002$. Panel D ($n > 3$ repeats/cell line), statistical analysis was performed using one-way ANOVA, and significance between groups was determined using Tukey's multiple comparison post hoc test, * $p < 0.05$, ** $p < 0.005$, *** $p < 0.005$, **** $p < 0.0001$.